DEEP

Innovation for:
De-Risking Enhanced
Geothermal Energy Projects

Deliverable

Deliverable 3.3 – Release of new hybrid models for induced seismicity forecasting

Report information	
Work package	WP3 Innovation in forecasting models and uncertainty quantification
Lead	ETH
Authors	Federico Ciardo, Victor Clasen, Antonio Pio Rinaldi & Luigi Passarelli
Reviewers	Laura Ermert
Approval	Stefan Wiemer
Status	Final
Dissemination level	Internal
Will the data supporting this document be made open access?	
If No Open Access, provide reasons	
Delivery deadline	30.11.2022
Submission date	30.11.2022
Intranet path	[DOCUMENTS/DELIVERABLES/Deliverable3.3.pdf]

This project has been subsidized through the Cofund GEOTHERMICA, which is supported by the European Union's HORIZON 2020 programme for research, technological development and demonstration under grant agreement No 731117.

Contents

Summary

This deliverable presents a newly developed suite of hydro-mechanical hybrid models for forecasting human-induced seismicity. The models are devised to be utilised in real-time or pseudo real-time applications, such as in the context of Adaptive Traffic Light System. We first present two simplified hybrid models that are based on axis-symmetric pore-fluid diffusion in a confined reservoir. The first model (HM0) accounts for linear pore-fluid diffusion, whereas the second model (HM1) includes the non-linear response of the medium upon injection of fluids. In both models, seismicity is triggered when the local pore-fluid pressure reaches a critical value according to Mohr-Coulomb failure criterion. Stochasticity is introduced either via an analytical statistical perturbation of the model parameters (hereafter CAPS), or via a stochastic earthquake simulator (hereafter SEED model). We apply these two models to the injection experiments at Bedretto Underground Laboratory and FORGE Test site and show that their forecasting capabilities are very promising when compared with other statistical models.

We also present a new three-dimensional hybrid solver for modeling induced-seismicity in fractured reservoirs. This is based on an equivalent continuum approach for fluid flow in fractured medium, in which fracture are mapped onto a computational grid and translated to properties of an equivalent medium. Seismicity, instead, is discretely modelled using an improved version of the stochastic SEED model. Overall and unlike previous similar models, here we can: i) Discriminate between seismic and aseismic deformations, ii) Assume a linear-weakening constitutive law for seed failure points and consistently a re-triggering mechanism (repeater earthquakes) based on local slip accumulation and iii) Introduce earthquake-earthquake elastic-stress transfer. We finally present some preliminary results associated with the 2022 16A stimulation at FORGE test site.

1 Introduction

Injection of fluids in fractured reservoirs triggers seismicity, as documented in many field injection experiments (Healy et al., 1968; Ellsworth, 2013; Zoback and Harjes, 1997; Grigoli et al. , 2017). The capability of forecasting human-induced seismic events prior to fluid injection is challenging due to the occurrence of many coupled and non-linear physical processes at depth. The time scales associated with these processes complicate further the picture: pore-fluid diffusion in a fractured reservoir may occur over time scales of days or months depending on the in-situ hydraulic properties of the medium, while transient energy dissipation associated with localized deformations can occur over a time scale ranging from a few seconds, in case of induced earthquakes, up to several months, in the case of slow aseismic slip.

Theoretical and numerical models have been developed and are still being developed by many research groups worldwide. Their goal is to get insight into these complex physical processes and provide suggestions that may help operators to design injection experiments and ultimately forecast seismicity with some confidence. The unsuccessful examples of injection-induced significant earthquakes of Basel (2006) (Deichmann and Giardini, 2009) and Pohang (2017) (Grigoli et al. , 2018) have further raised the importance of having reliable models so as to avoid that similar projects could potentially be terminated again in the future.

Within the Adaptive Traffic Light System (ATLS) approach, a data-driven seismic risk mitigation tool (Grigoli et al. , 2017; Mignan et al., 2017), induced-seismicity should be forecasted in *real-time* or *pseudo real-time* based on continuously acquired data, in order to adapt seismic hazard and risk calculation and assess in real time the safety of the future injection operations and/or modulate these latter to reduce the risk. A challenge of the ATLS is related to the forecasting performance of the adopted model(s). Generally speaking, the more complex the model, the larger the computational cost associated with it. Pure physics-based models that account for all the coupled physical processes are very reliable yet computationally expensive and with many parameters to calibrate. Restricting here to hydro-mechanical (HM) models, the numerical resolution of quasi-static or dynamic balance of elastic momentum in the reservoir is by far the most expensive operation due to its highly non-linear coupling with pore-fluid propagation and possible weakening mechanisms. Although the computing power is continuously increasing in time, with the processing power of computers that doubles every two years (Moore's law), the feasibility of reliably calibrating pure physics-based models

for real-time or pseudo real-time forecasting of seismicity is still limited if not impossible. Hybrid models, which are partially physics-based and partially statistical-based, are instead more attractive for ATLS-type approaches due to their lower computational cost. The balance of elastic momentum in these models is replaced by a stochastic model for deformations, resulting in a faster forecasting of seismicity (if any).

Over the past years, several hybrid models for forecasting induced-seismicity have been proposed (see Bechmann et al. (2012); Gischig and Wiemer (2013); Goertz-Allmann and Wiemer (2013); Rinaldi and Nespoli (2017); Zbinden et al. (2020); Karvounis and Wiemer (2022); Ritz et al. (2022) to cite a few). Despite these numerous efforts, some of their assumptions limit their applicability and could be extended to better model the physical processes, while keeping their complexity low. In this deliverable, we present a new developed suite of hybrid models that are geared towards a fast and reliable forecasting of seismicity for real-time or pseudo real-time applications. In the first part of this deliverable, we present two simplified hydro-mechanical hybrid models and their applications to BedrettoLab (Bedretto Underground Laboratory for Geosciences and Geoenergies) and Utah FORGE injection experiments. We then move on to a more complex 3-dimensional hybrid model that accounts for a network of pre-existing fractures, that could be used for verification or to construct synthetic datasets.

2 One-Dimensional hybrid hydro-mechanical models

We developed a suite of simplified hybrid hydro-mechanical models driven by the need of hybrid solvers that can efficiently forecast fluid-driven seismicity for real-time applications. These models couple linear and non-linear pore-fluid propagation in a reservoir with stochastic or analytical model for seismicity nucleation. The coupling is only one-way, in a sense that pore-fluid perturbation affects seismicity nucleation but not vice-versa.

In this class of models, we assume axis-symmetric pore-fluid diffusion from vertical injection wellbore in a bounded reservoir of thickness h. The fluid mass conservation equation in terms of pore-fluid pressure p can be written in radial coordinates as

$$\rho S \frac{\partial (p - p_o)}{\partial t} + \frac{1}{r} \frac{\partial}{\partial r} \left(\frac{\rho \cdot k \cdot r}{\mu} \frac{\partial (p - p_o)}{\partial r} \right) = Q, \tag{1}$$

where ρ is the fluid density $\left[ML^{-3}\right]$, μ is the kinematic fluid viscosity $\left[ML^{-1}T^{-1}\right]$, k is the permeability of the medium $\left[L^2\right]$, $S = \phi\beta$ $\left[M^{-1}L^1T^2\right]$ is a storage coefficient that combines fluid and pore compressibilities β as well as porosity ϕ, and Q is a source term representative of point injection at a given mass rate per unit volume $\left[MT^{-1}L^{-3}\right]$. Depending on whether the permeability of the medium is a constant quantity or evolves as function of local pore-fluid pressure, Equation (1) can be either a linear or non-linear partial differential equation for the unknown pore-pressure field $p(r, t)$. Its resolution may thus be obtained analytically or numerically.

We have developed two hybrid models that account for both scenarios and will present in the following sections: HM0 that is based on linear pore-fluid diffusion in the medium and is suited when large non-linearities do not arise upon fluid injection at depth; and HM1 that is devised to account for non-linearities that may arise when large quantities of fluid are injected into a fractured reservoir In both HM0 and HM1 model, fluid-driven seismicity can be modelled using either a stochastic approach (seed model) or an analytical simplified solution. In the following section, we present further details.

2.1 HM0/1

In the first simplified hybrid model (HM0), we assume that all the fluid and medium scalar properties are constant. Using appropriate initial and boundary conditions, Equation (1) can be solved *analytically* for the spatial-temporal evolution of pore-fluid pressure $p(r, t)$ along the radial distance r. The analytical solution,

known as Theis' solution, reads

$$p\left(r,t\right)-p_o\left(r\right)=-\frac{\mu}{4\pi kh}\left(\sum_{j=1}^{N_j}\Delta q_j \mathrm{E}_i\left(-\frac{r^2\mu S}{4k(t-t_j)}\right)\right), \tag{2}$$

where E_i is the Exponential integral function. Note that pore-pressure solution is given by the superimposition of analytical solutions associated with each increment of injection rate Δq_j and elapsed time $t-t_j$ (from each change of injection condition). The analytical pore-pressure distribution at current time $t+1$ is then used to evaluate stochastically the seismicity (either using the seed model or via the CAPS analytical solution - see below).

The second simplified hybrid model (HM1) accounts for non-linear pore-fluid propagation in the reservoir. Laboratory and field experiments have shown that injection of fluids in fractured reservoir leads to localized elastic and inleastic deformations along pre-existing geological discontinuities (i.e. fractures/faults). These mechanically-induced deformations do affect pore-fluid propagation. Shear-induced dilatancy, for instance, is manifested with an increment of hydraulic fractures aperture based on local shear deformations, and thus an increment of permeability. According to the cubic law, which is commonly used for modeling fracture transmissibility, as permeability enhancement scales quadratically with fracture aperture. It is reasonable to think, therefore, that such a non-linear dependency does affect pore-fluid propagation and hence seismicity nucleation.

In this model, we consider a pressure-dependent permeability and re-write Equation (1) as:

$$\rho S\frac{\partial\left(p-p_o\right)}{\partial t}+\frac{1}{r}\frac{\partial}{\partial r}\left(\frac{\rho\cdot k\left(p\right)\cdot r}{\mu}\frac{\partial\left(p-p_o\right)}{\partial r}\right)=Q \tag{3}$$

According to the cubic law, the permeability of a fractured medium reads

$$k\left(p\right)=\frac{w_h^2\left(p\right)}{12}, \tag{4}$$

where w_h is the fractures aperture that depend on local increase of pore-fluid pressure via the Barton-Bandis model (Barton et al., 1985):

$$w_h\left(p\right)=a_o-\frac{\sigma_n'}{K_n+\frac{\sigma_n'}{a_o-a_r}} \tag{5}$$

with a_o and a_r being the aperture at zero effective normal stress $\sigma_n'=\sigma_n-p$ and its residual value respectively, and K_n the fracture normal stiffness.

Using a finite difference scheme for spatial discretization together with a Backward Euler time integration, Equation (3) reduces to a linear system of equations in the form

$$A\cdot p^{t+1}=b, \tag{6}$$

which can be readily solved for the current radial pore-fluid pressure distribution. A and b are respectively the finite difference (sparse) matrix and the right-hand side vector that includes the injection boundary condition. The current pore-pressure field is then given to one of the following pressure-based seismicity model.

SEED model The first seismicity model follows the seed model approach introduced by Goertz-Allmann and Wiemer (2013) and Gischig and Wiemer (2013). Here, seed points are potential earthquakes that are randomly placed in space. Stress conditions and friction properties fluctuating in a random manner from the average stress field are assigned to each seed. Using Mohr-Coulomb yielding criterion, a failure pressure p_f is calculated for each of the seeds and evaluated with the current pressure solution at each distance from injection point, through the following equation:

$$p_f=c/f+\sigma_n'-\tau/f \tag{7}$$

where c is the cohesion, f the friction coefficient, σ'_n the effective normal stress, and τ the shear stress. If the difference between the transient fluid pressure at the seed and its failure pressure is positive, an earthquake is triggered and a drop in shear stress $\Delta\tau$ is applied.

Converting Any Pressure Solution to Seismicity (CAPS) The other pressure-based seismicity model is based on an analytical stochastic approach that also accounts for the Mohr-Coulomb failure criterion. Assuming that the rock strength parameters (i.e. friction coefficient and cohesion) are constant and in-situ principal stresses are normally distributed, with mean values equal to the measured values and an associated standard deviation σ, the total tractions along the critical orientation[1]

$$\theta_c = \pi/4 + \text{ArcTan}\left(f\right)/2 \tag{8}$$

can be obtained as

$$\begin{aligned} \sigma_n &= \frac{1}{2}\left(\sigma_1 + \sigma_3\right) + \frac{1}{2}\left(\sigma_1 - \sigma_3\right)\cos\left(2\theta_c\right) \\ \tau &= \frac{1}{2}\left(\sigma_1 - \sigma_3\right)\sin\left(2\theta_c\right) \end{aligned} \tag{9}$$

The in-situ effective normal stress is then given by $\sigma'_n = \sigma_n - p_h$, where p_h is the hydro-static pressure. σ_n and τ in (9) are two scalars that are evaluated analytically and they are normally distributed due to their dependence on σ_1 and σ_3. We use these normal distributions to compute the analytical Cumulative Density Function (CDF) and Probability Density Function (PDF) of hypocenters being reactivated at a certain pressure p_f (obtained from (7)), considering the hydrostatic conditions at each radius. The standard deviation associated with p_f is given by

$$\sigma_{p_f} = \sqrt{\sigma_{\sigma_1}^2 \frac{\left(1 + \cos\left(2\theta_c\right) - \frac{\sin(2\theta_c)}{\mu}\right)^2}{4} + \sigma_{\sigma_3}^2 \frac{\left(1 - \cos\left(2\theta_c\right) - \frac{\sin(2\theta_c)}{\mu}\right)^2}{4}} \tag{10}$$

2.2 HM0/1 verification and seismicity models' comparison

In this section, we verify the implemented numerical fluid flow solution with synthetic data comparing it to the exact analytical solution (Theis' solution) in equation 2 in subsection 2.2.1 and we compare the performance of both the CAPS and seed models using the same synthetic dataset in subsection 2.2.2.

2.2.1 Numerical flow model verification

We show one test based on the synthetic injection flow rate given in Figure 1 panel a). Here, fluid is injected into a 8-m open borehole interval (see simulation parameters in Table 1) following a step-wise increasing injection strategy. The injected flow rate is increased every two hours starting 120 minutes after initiating the simulation until shut-in 10.5 hours after the injection operation started. We implement a non-uniform spatial discretization with logarithmically increasing spacing between the nodes (101 nodes, 100 elements) with increasing distance form the injection point. Further, we assume a constant hydro-static pressure condition and no-flux boundary conditions (neither at the point of injection nor at the far field, at 1000 meters from the point of injection). Using further parameters listed in Table 1, the results of the flow models are shown in Fig. 1.

Fig. 1 panel a) shows the injection protocol as well as the three pressure solutions (HM0 analytical, HM0 numerical, and HM1 solutions) at the point closest to injection, panels b)-f) and c)-g) shows the time and spatial profiles for the HM0 and HM1 pressure solutions, respectively. The temporal and spatial behavior of the non-linear pressure solution varies with respect to the linear solutions according to the additional hydraulic parameters introduced to account for variability in the permeability parameter. Both the analytical and numerical approaches to solve the linear pressure solution match quite well, as it is shown in panels b)

[1]Note that we use only one value of critical orientation and neglect its conjugate. This is because all the shear tractions are assumed to be positive (i.e. $\sigma_1 > \sigma_3$).

Table 1: Input parameters for synthetic test.

Symbol	Description	Value
Hydraulic properties		
k_f	Permeability (const. for HM0)	$5 \cdot 10^{-15}$ [m^2]
S	Storage	10^{-11} [1/Pa]
μ	Fluid kinematic viscosity	10^{-3} [Pa $\cdot$ s]
ϕ	Porosity	$4.2 \cdot 10^{-2}$ [–]
h	Interval thickness	8 [m]
HM1		
σ_n	Normal stress	21 [MPa]
K_n	Fracture normal stiffness	10^{14} [Pa/m]
a_o	Aperture at zero eff. normal stress	$8 \cdot 10^{-4}$ [m]
a_r	Residual aperture	10^{-8} [m]
Geomechanical properties		
σ_1	Maximum principal stress	26 [MPa]
σ_3	Minimum principal stress	15 [MPa]
σ_{σ_1}	Standard deviation of σ_1	10%σ_1 [MPa]
σ_{σ_3}	Standard deviation of σ_3	10%σ_3 [MPa]
c	Cohesion	2 [MPa]
f	Friction coefficient	0.6 [–]
In-situ conditions		
p_h	Hydro-static pressure	11.6 [MPa]
Simulation parameters		
t_{init}	Initial time	0. [h]
t_{end}	End time	20.5 [h]
t_{shut}	Shut-in time	12. [h]
Δt	Time step	1. [min]
	Seed density	variable [–]

and f) in Figure 1 where the analytical solution is plotted on top of the numerical solution for five different points in space and moments in time. Also, panel d) shows that the relative error in pressure is lower than 10% for most times until shut-in, although it increases considerably at larger distances from the injection point (panel e)).

2.2.2 Synthetic model to compare the CAPS and seed models' performance

We use the same synthetic model as in the previous subsection to simulate the seismicity using both seismicity models described in section 2.1. The flow and seismicity models are sequentially coupled. Hereby, the pressure changes computed in the flow model (here we use Theis' solution) affect the seismicity model but the triggered seismicity does not change the pressure solution (e.g. via permeability increase) for the next time step. Along with the pressure solution we input the geomechanical parameters listed in Table 1 to simulate seismicity during the 20.5-hour simulation, as it is shown in Figure 2. We perform three simulations with increasing number of seeds in space (panels b)-d)) and see that the seed model matches the CAPS model better if the number of seeds is high enough. It is important to note that for the synthetic results presented in Figure 2, no re-triggering of seeds was considered (the seeds are only allowed to trigger once, then they are discarded) and only one simulation was performed for each change in seed number, providing a deterministic result in terms of seismicity rate.

2.3 Application to BULGG

We apply the hybrid models described in section 2.1 to the first collected dataset of a full-scale hydraulic stimulation performed in November 2020 at the Bedretto Underground Laboratory for Geoenergies and

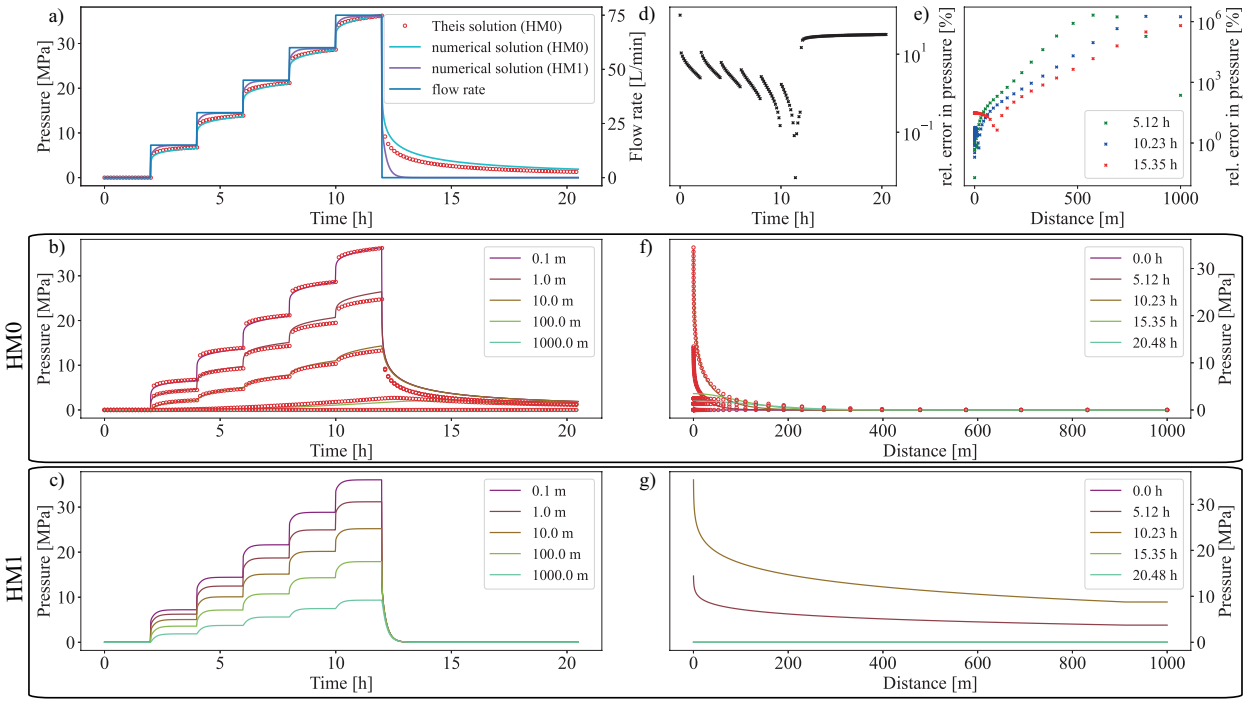

Figure 1: Visualization of the different pressure solutions discussed in section 2.1 following the synthetic injection flow rate in blue in panel a), which also shows the pressure evolution in time at the point of injection for Theis' analytical solution (red scatter points), the HM0 numerical solution (light blue), and the HM1 solution (purple). The spatial and temporal evolution of the pressure solutions for five different points in space and time moments, respectively, are shown in panels b) and f) for the HM0 class (the analytical solution as red scatter points on top of the numerical solution) and in panels c) and g) for the HM1 solution. Panel d) shows the relative error (in percentage) of the numerical solution (HM0) w.r.t. the analytical solution in time for the point closest to injection. Panel e) shows the same but in terms of distance from the injection point for three different time moments.

Geosciences (BULGG)[2]. The hydraulic and seismic datasets presented in Figure 3 were collected during an approximate 34-hour-long injection operation into a 8.5 meter open interval section located at roughly 1270 meters above sea level. The observed magnitude range shows mainly picoseismic events (-5 < M_w < -2), with just 5 microseismic events (-2 < M_w < 2) out of a total of 383 recorded events.

2.3.1 History matching and seismicity forecast

As a first step towards evaluating the forecasting performance of these 1-D hybrid models, we split both the hydraulic and the seismic datasets in two phases: the training (or fitting) phase and the forecasting (or validation) phase, marked as number one and two in Figure 4 - panels (a-b). As mentioned before, the flow and seismicity models are sequentially coupled. During the training phase, the flow model is fed with the injected flow rate (blue continuous line in Figure 4) and with the known hydraulic parameters. Via inverse modelling, we calibrate for a selection of unknown or uncertain hydraulic parameters and fit the observed pressure (red continuous line in Figure 4) to the computed pressure solution. We optimize our pressure solution using the Differential Evolutionary Algorithm (DEA, Storn and Price, 1997), a global optimization algorithm that finds the optimal parameters within a pre-defined uncertainty range minimizing a tailor-made cost function. Then, the fitted pressure solution serves as an input to the seismicity model along with the observed seismicity (Fig.3-b)). The solution in terms of seismicity rate (Fig. 4) is fitted to the observations while calibrating for geomechanical parameters within a pre-defined uncertainty range. Once the pressure and seismicity solutions are fitted to the observations for the duration of the training phase (here the first 15 hours from injection), the calibrated parameters are used to issue a forecast for the upcoming time in terms of a pressure and seismicity rate based on the flow rate in the validation phase.

[2]BULGG is an underground research laboratory located in Bedretto (Ticino), Switzerland (`http://www.bedrettolab.ethz.ch/en/home/`)

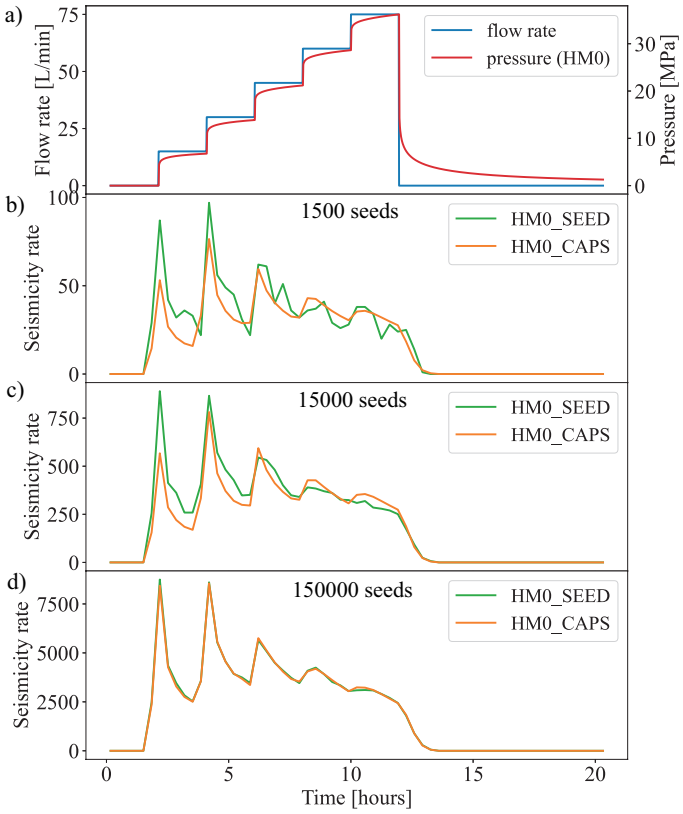

Figure 2: Visualization of the seismicity models' performance based on the analytical pressure solution (Theis' solution; red in panel a) and same as red scatters in Figure 1 panel a)) from the synthetic injection flow rate (blue in panel a) and same as in Figure 1 panel a)). Panels b)-d) compare how the CAPS (orange) and seed model (green) perform with increasing number of seeds.

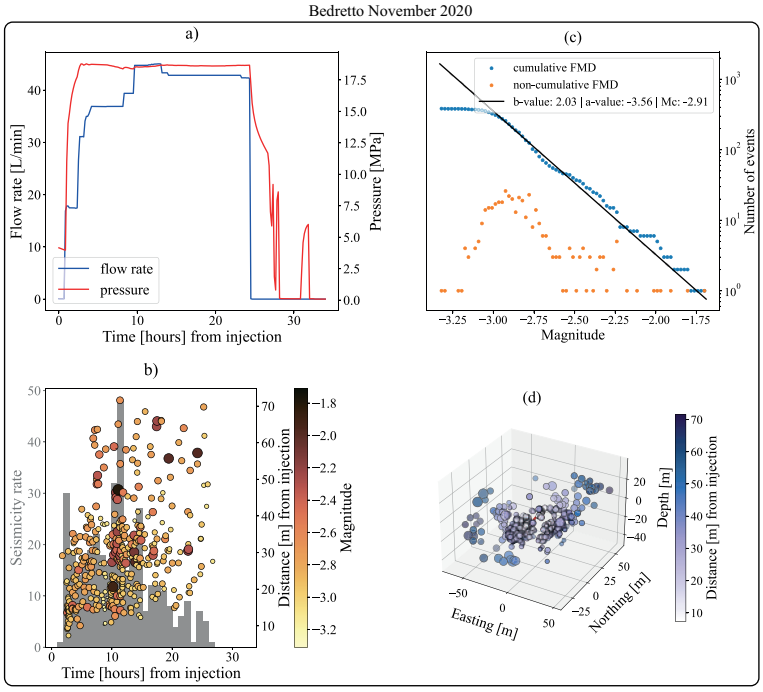

Figure 3: Bedretto November 2020 hydraulic stimulation raw data: a) Injection flow rate (blue) and recorded pressure (red). b) Seismicity rate (events per hour) and events with time, distance, and magnitude (colorbar). c) Frequency-magnitude distribution of all earthquakes in the catalog. d) Spatial distribution of the seismic events in the targeted volume.

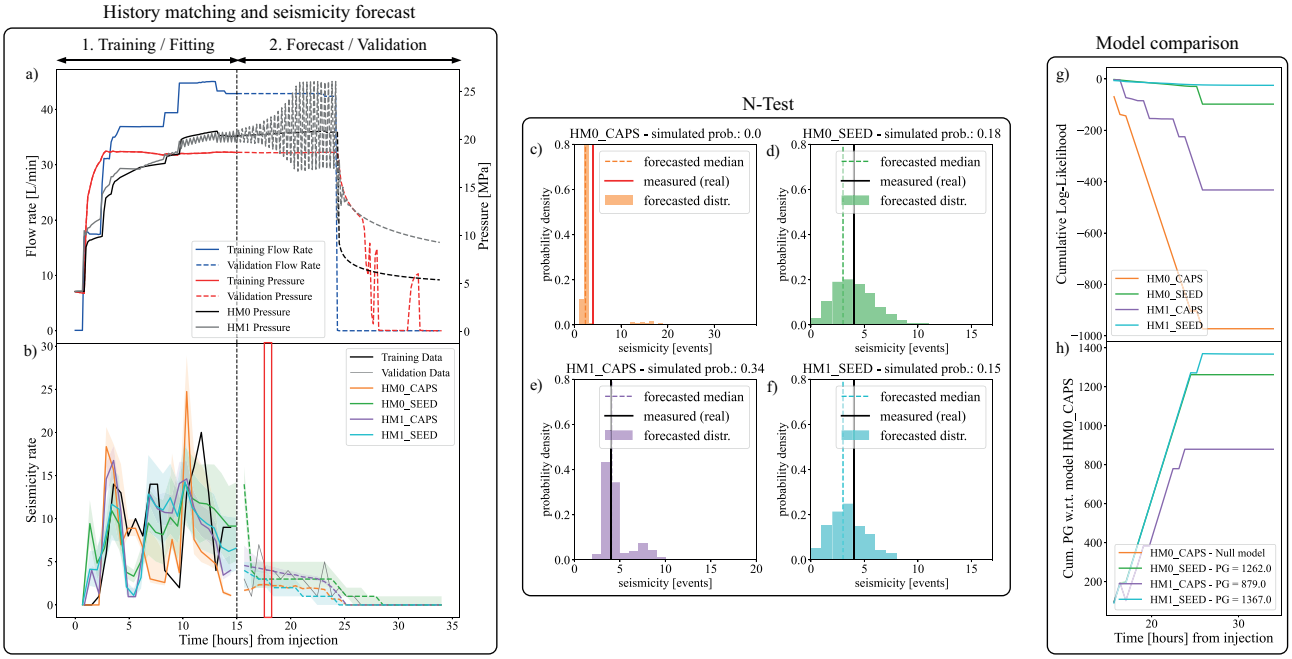

Figure 4: Application of all four hybrid models to the Bedretto dataset: a) Injected flow rate along with the observed pressure and the pressure solutions for HM0/1. b) Observed seismicity rate along with fitted (1. Training / Fitting) and forecasted (2. Forecast / Validation) seismicity. c)-f) N-Test for the time moment marked in b) for the four models. g) Cumulative log-likelihood value for the four models throughout the validation phase. h) Same as g) but for the cumulative probability gain (PG).

2.3.2 Uncertainties estimation and model simulations

As it is currently implemented, the seed model accounts for its parameters' uncertainties by randomly assigning different failure pressure limits to the distributed seeds sampling from a normal distribution with mean and standard deviation in accordance to pre-defined background stress conditions and friction properties. We run a multiple number of simulations N_{sim} to issue probabilistic forecasts (distribution of possible seismicity rate solutions). The analytical model is deterministic and therefore produces a single forecast based on the optimal parameters. We account for the model parameters uncertainties by sampling N_{sim} times from normal distributions of selected parameters (e.g. standard deviations of the principal stresses) whose mean corresponds to their optimal value and standard deviations are fixed. By running a certain number of simulations we are able to issue multiple synthetic catalogs and account for the uncertainties of the model parameters making the models probabilistic, as shown in Fig. 4 b) dashed lines for the median and shaded area for the 95% confidence interval (CI) of the distribution for the different model classes.

2.3.3 Testing

In order to assess how the model actually performs, we check how well the forecasted seismicity rate distribution matches the observations during the validation phase (Zechar et al., 2010). Kagan and Jackson (1995) introduced the N-Test, which assigns probabilities to each seismicity rate bin according to its distribution for a given time interval of the validation phase. This is shown in Fig. 4 panels (c) and (f) for the four different model combinations at the time moment marked with a red rectangle in Fig. 4-b in the validation phase, where the histogram shows the probability density distribution of the seismicity rate, the dashed vertical line its median, and the vertical straight line the observed seismicity.

The N-Test is defined such that a model passes it if the observed seismicity lies within the 95% CI of the forecasted probability density distribution for a given time interval. For the time moment shown in the mid panels in Fig. 4-c-f, the HM0_CAPS model would be the only one to fail the test, while the HM1_CAPS would be the better performing model since its probability to reproduce the observed rate is highest (0.34).

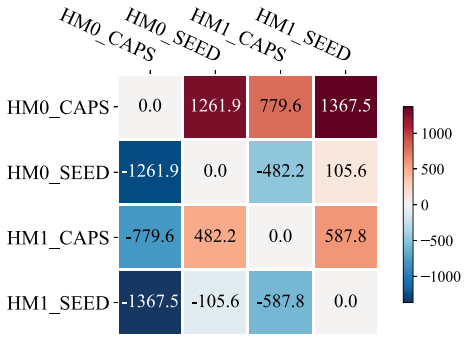

Figure 5: Heatmap showing the cumulative PG of each model against each other (the rows serving as null models) towards the end of the validation phase with red showing high values of PG.

2.3.4 Model comparison

The term probability gain (PG) is introduced as a measure of forecasting performance of a model against another model. Based on the approach of Kagan and Knopoff (1987), who proposed to calculate the PG as the difference between the log-likelihood of two given statistical models, Passarelli et al. (2010) proposed to assess the forecasting performance of any model (accounting not only for statistical models) by directly computing the probability of forecasting the observed rates and compare them via PG, which is simply calculated as the difference of the "likelihoods" of the probability of two models

$$PG = \left(l_A(\widehat{\theta} \mid H_f) - l_B(\widehat{\theta} \mid H_f)\right) / \ln(2) \tag{11}$$

where the l_i of model i (with i being e.g. model A or B) is calculated by taking the natural logarithm of the probability for the model i to reproduce the observed (future) seismicity rate, H_f, for a given time interval

$$l_i\left(\widehat{\theta} \mid H_f\right) = \ln\left(\Pr\left(\text{model}\, i \mid \widehat{\theta}, H_f\right)\right) \tag{12}$$

where $\widehat{\theta}$ represents the optimal choice for the model parameters.

Fig. 4-g shows the cumulative of Eq. (12) for all model combinations and Fig. 4-h shows the cumulative of Eq. 11 taking the HM0_CAPS model as reference model (or null-model). Then, if we want to know which model actually performs better (on average) throughout the full validation phase, we can compute the cumulative PG at the end of the validation phase for all possible combinations of models for A and B in Eq. 11 and represent it as a heatmap, as shown in Fig. 5. Therefore, although HM1_CAPS is the better performing model for the time moment shown in the red rectangle in Fig. 4 b) and in the N-Test, the HM1_SEED model is the overall better performing model since its cumulative PG is always positive against any other model (see Fig. 5).

2.4 Application to FORGE 2019 stimulation

Before the April 2022 injection experiment at FORGE test site, a team was asked to perform an a-priori risk assessment. In order to provide synthetic seismic data for the risk assessment, we generated a set of catalogs using the HM0-Seed hybrid model previously described. Notably, we calibrated the model parameters using the available injection and seismic data of the 2019 stimulation at the vertical well 58-32 (intervals 1, 2 and 3). In Figure 6, we report the comparison between the model results and the observed data, for both wellhead pressure (left) and cumulative number of events above the magnitude of completeness M_c (with 20 stochastic realizations). We can observe that the hybrid model fits reasonably well the observed pressure, despite the use of a hydraulic model with no permeability changes (HM0). Some discrepancies are visible for the rate of seismicity, although the final number of simulated events is similar to observations. Using the fitted parameters (cohesion, friction coefficient, stress drop coefficient and seed density), we ran a forward forecasting of seismicity using the planned injection protocol of the 2022 stimulation (although the actual stimulation protocol deviated from the planned one) and generated 100 catalogs. The resulting forward

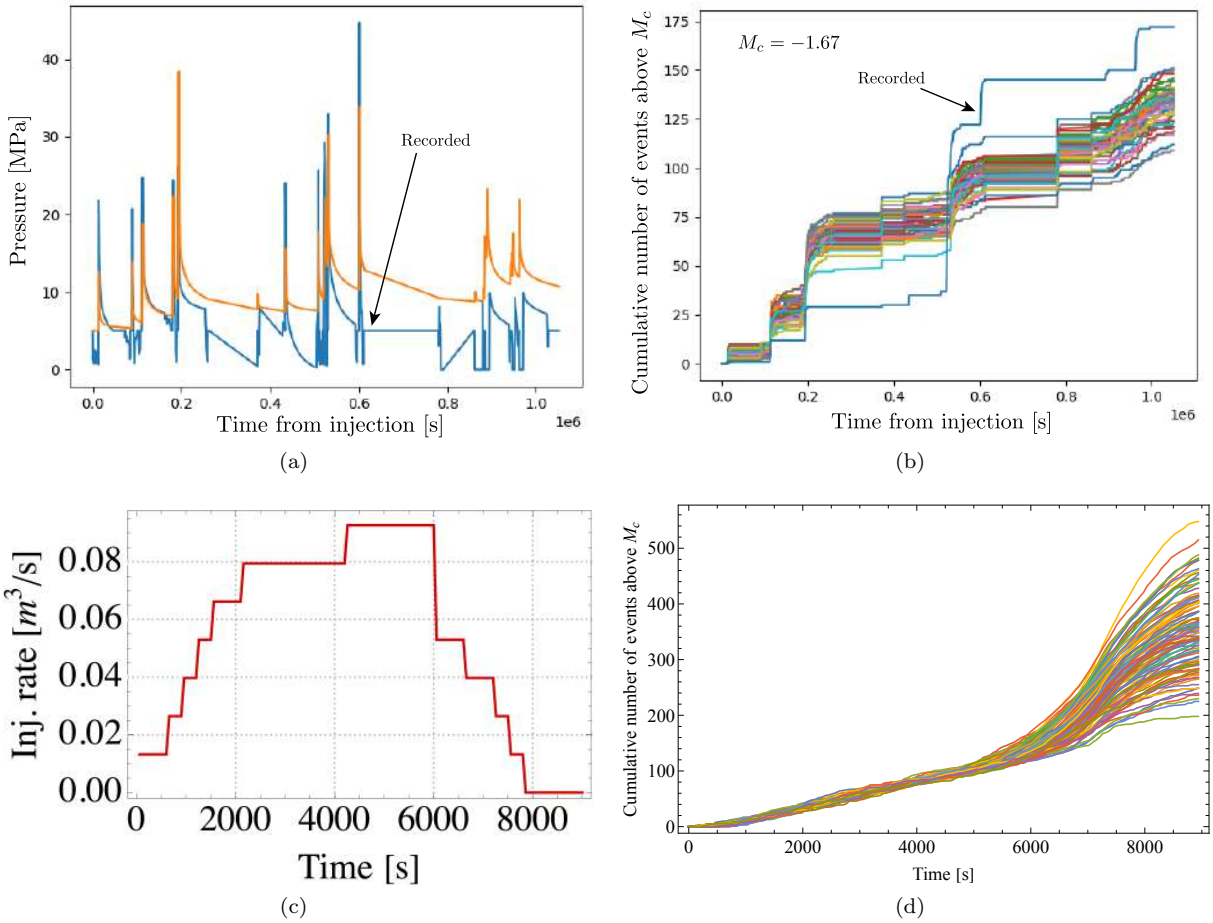

Figure 6: Top: Comparison between observations and model fit results for wellhead pressure (left) and cumulative number of events (right) at FORGE. The model used is HM0-Seed. Bottom: Injection strategy used for forecasting events (left) and cumulative number of events for the generated 100 catalogs (right).

model resulted in total number of events between 200 and 500, given the assumed injection plan.

3 Three-Dimensional hydro-mechanical hybrid model

We now present a newly developed hybrid hydro-mechanical 3D model that account for non-linear pore-fluid propagation in fractured reservoir and seismicity nucleation. Before doing that, we describe the reasons that have brought us to develop from scratch this solver.

As mentioned in the DEEP proposal, the original plan was to enhance the current version of an in-house developed hybrid solver called HFR-Sim, with the ultimate goal of embedding it into the ATLS chain. Although it was in principle doable, we found out that such a solver is not really suitable for modelling injection-induced seismicity in the FORGE injection experiments. In the following section, we present several tests we have performed with HFR-Sim and highlight the associated problems.

3.1 HFR-Sim tests

HFR-Sim is a 3D hybrid numerical solver devised for modelling fluid induced seismicity. It includes a deterministic module for transient pore-pressure evolution in a fractured rock mass based on an adaptive Hierarchical Fracture Representation (a-HFR) (Karvounis and Wiemer, 2022). Fractures are explicitly modelled and are characterized by constant hydraulic properties (constant permeability and aperture). Linear single-phase fluid flow in fractures and solid mass is numerically solved using a Finite Volume scheme together with a Backward Euler time integration method. Seismicity, instead, is modelled using the seed model, which is the same as the one described above with the only difference that the full 3D stress tensor formulation is taken into account (see Karvounis and Wiemer, 2022, for full details).

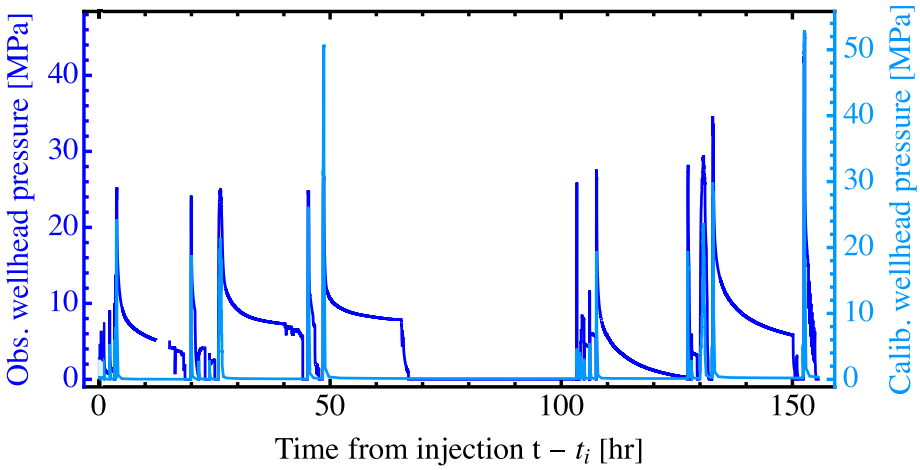

Figure 7: Comparison between observed (dark blue) and calibrated (light blue) wellhead pressure using HFR-Sim and the dataset of the April 2019 FORGE stimulation.

Due to the lack of verification tests for the fluid flow solver, we ran a number of simulations to check the accuracy of the numerical solver. To do so, we first removed the Paceman well model and introduced the simpler point source type of injection. We then ran the following verification tests: i) steady-state pore-pressure variation in a 3D homogenous unfractured medium and ii) point injection at constant volumetric rate in a 3D homogenous unfractured medium, for different mesh discretizations (to check the mesh-dependency problem that was found to be present with Paceman well model). Upon fixing a convergence problem in the iterative solution of the governing system of equations, we obtained a good match between numerical and corresponding analytical solution (see their expression in Carslaw and Jaeger, 1959).

We then created a model for the 2019 stimulation at FORGE Test site. Notably, we developed an ad-hoc 3-dimensional discrete fracture network generator for HFR-Sim and created a Discrete Fracture Network representative of the FORGE test site (based on the available FMI logs data). We manually calibrated the model parameters using the hydraulic and seismic data of the 2019 stimulation (see Figure 7), and ran a forward forecast of seismicity based on the injection data of the 2022 stimulation. Although the calibration was quite successful (shut-in phase excluded), the forecasting was clearly not, with an unphysical pore fluid over-pressure near injection point and the nucleation of a large number of seismic events (more than 20×10^3). This is because the injected volumes over the time scales of injections are very different between the 2019 and 2022 stimulations (at least of one order of magnitude), as reported in the first DEEP annual meeting. The model linearity and thus the lack of inelastic changes of DFN permeability with local pore-pressure during continuous injection leads to such unphysical hydro-mechanical response. This is also strengthened by the evidence that the 2022 stimulation was a hydraulic fracturing type of stimulation, with a pressure response of stage 3 that clearly suggest the nucleation and propagation of a penny-shape crack (which then triggered other events due to its interaction with pre-existing fractures). The permeability of an hydraulic fracture is strongly non-linear due to its cubic dependency on fracture aperture (cubic law). Being able to capture this non-linear phenomenon is extremely important and with the current version of HFR-Sim this is not possible to achieve. The inclusion of non-linear permeability changes in such a model is not trivial, since a non-linear solver must be implemented for the implicit solution of spatial and temporal evolution of pore-fluid pressure. This would require a complete change of code architecture, which - in the end - would lead to a re-write of the whole flow solver.

These considerations have brought us to develop a new hybrid solver for induced-seismicity forecasting in fractured rock masses that extend previous similar solvers. In the following sections, we present it and showcase its preliminary application to the FORGE 2022 stimulation.

3.2 HMStat: a new 3D hybrid model for verification and generation of synthetic data-sets

3.2.1 Equivalent Continuum Model for flow in fractured porous media

We adopt a single continuum approach to represent fractures in the porous medium, geared towards a fast approach that can forecast injection-induced seismicity driven by pore-fluid propagation in a naturally fractured reservoir. Notably, we adopt an Equivalent Continuum Modeling approach in which fractures are translated into properties of an equivalent porous medium. A fractured rock mass behaves similar to a homogeneous and anisotropic porous medium if it behaves as a representative element volume (REV) (Long et al., 1982). This means that the effective/equivalent medium properties (permeability and porosity for instance) do not vary considerably with the reference length-scale of the system, although this condition might not always be satisfied due to the lack of scale separation in natural fractured systems (Berre et al., 2019). This approach has been widely used in literature and numerous studies have shown that the representation of a discrete fracture network with a sufficiently resolved grid of equivalent continuum blocks allows to reproduce well its percolation behaviour that would be obtained with discrete fracture network conceptual models (e.g. Jackson et al., 2000; Svensson, 2001; Leung et al., 2012; Hadgu et al., 2017; Sweeney et al., 2020; Kottwitz et al., 2021)).

Assuming that there exist a REV for a three-dimensional naturally fractured rock mass, single-phase isothermal fluid flow at the continuum scale is governed by the fluid mass conservation equation

$$\frac{\partial\left(\rho\langle\phi\rangle\right)}{\partial t}+\nabla\cdot\left(\rho\langle\mathbf{v}\rangle\right)=q\delta\left(x_{inj},y_{inj},z_{inj},t\right), \tag{13}$$

where ϕ is the unitless rock porosity $[-]$, ρ is the fluid density $\left[ML^{-3}\right]$, q is a source term (mass rate per unit volume) representative of an injection at point $(x_{inj},y_{inj},z_{inj})$ and $\mathbf{v}$ is the average fluid flux given by Darcy's law

$$\langle\mathbf{v}\rangle=-\langle\frac{\mathbf{K}}{\mu}\nabla\left(p-p_o\right)\rangle \tag{14}$$

In Equation (14), $\mathbf{K}$ is the permeability tensor $\left[L^2\right]$, μ is the (constant) dynamic fluid viscosity $\left[ML^{-1}T^{-1}\right]$ and $\bar{p}\left(x,y,z,t\right)=p\left(x,y,z,t\right)-p_o\left(x,y,z\right)$ is the pore-fluid over-pressure with respect to the initial (ambient) value p_o. Note that gravity is neglected and the angular brackets $\langle\cdot\rangle$ denote the average quantity over a suitable rock volume that contains fractures and porous matrix. This volume can be either the entire fracture system volume or the grid block used in the computational domain (Berre et al., 2019). In our approach, we assume that the rock mass properties (permeability and porosity) are averaged over the simulation grid block and define these properties as *equivalent grid-block properties* in line with the nomenclature given by Durlofsky (1991). These quantities are distributed heterogeneously in the medium and mimic the presence of a discrete fracture network. One of the most crucial aspect of the single continuum-based approach is thus the capability of the equivalent grid-block properties to reflect the anisotropic flow at the scale of the continuum cells. Several techniques have been proposed in the literature to generate equivalent continuum models of discrete fracture network, both in 2D (Samardzioska and Popov, 2005; Botros et al., 2008; Reeves et al., 2008; Rutqvist et al., 2013; Chen et al., 2015; Gan and Elsworth, 2016) and in 3D (Lee et al., 2002a; Hadgu et al., 2017; Sweeney et al., 2020). The so called Oda's crack tensor theory (Oda, 1986) is perhaps the most widely used due to its simplicity and is adopted in our approach as well. According to this theory, fractures are considered as disk-shaped entities embedded in a 3D grid domain. A grid cell (or block) that is intersected by one fracture is assigned a permeability tensor that is aligned with the orientation of the intersecting fracture. For multiple fractures intersection, the permeability tensors associated with each fracture are summed up, leading to a unique positive definite symmetric tensor for the fractured cell. Mathematically, this translates to

$$k_{ij}=\frac{1}{12}\frac{1}{V^e}\sum_{f=1}^{N^f}A^f\left(w_h^f\right)^3\left(\left(\hat{n}_{kk}^f\right)^2\delta_{ij}-\hat{n}_i^f\hat{n}_j^f\right), \tag{15}$$

where k_{ij} are the ij-entries of the fractured permeability tensor, $A^f=\pi\left(R^f\right)^2$ is the area of the f-th fracture

intersecting the cell e of volume V^e, characterised by a radius R^f, hydraulic aperture w_h^f and orthonormal vector $\hat{\mathbf{n}}^f$ that identifies uniquely its orientation in the 3D domain. Note that the permeability tensor arising from (15) is very similar to the one proposed by Chen et al. (1999), with the fracture coordinate transformation tensor that is exactly the same in both approaches. Note also that when a fracture orientation is not aligned with the grid directions, the permeability tensor of fractured grid blocks is dense and anisotropic.

Following the work of Hadgu et al. (2017) and Sweeney et al. (2020), the equivalent porosity for a fractured grid-block is defined as

$$\phi = \sum_{f=1}^{N^f} \frac{V^f}{V^e}, \tag{16}$$

where $V^f = A^f w_h^f$ is the volume of fracture f in cell e and the summation is still defined over all the fractures intersecting that cell.

It is worth mentioning that this equivalent continuum modeling approach is based on two fundamental assumptions: i) the element volume over which the equivalent properties are calculated must be a REV and ii) that fluid flow occurs only within the discrete fracture network, i.e. the matrix permeability is much smaller than the ones of pre-existing fractures. In order to fulfill the second assumption, in this contribution we assume that the permeability tensor of the unfractured grid-blocks (denoted by a superscript *) is isotropic and given by

$$k_{ij}^* = k_m \delta_{ij}, \tag{17}$$

where δ is the Kronecker delta and k_m is the matrix permeability value that is always much lower than any k_{ij}. As far as the matrix rock porosity ϕ^* is concerned, a typical value for low permeability rocks, such as granite, is assigned to each unfractured grid block.

In an event of fluid injection in deep and highly fractured rock masses, the fractures that act as major conduits for pore-fluid propagation experience changes in permeability due to local changes of effective normal stresses, as supported by many laboratory studies (e.g. Brace, 1978, 1980; Huenges and Will, 1989). In order to comply with this non-linear process, we assume that the equivalent permeability tensor of fractured elements changes with average local effective normal stress as

$$k_{ij} = k_{ij} + \Delta k, \tag{18}$$

where the increment of permeability Δk is calculated using the effective stress-dependent permeability law introduced by Rice (1992) (written in incremental form)

$$\Delta k = k_* \mathrm{e}^{-\langle \sigma'_{n,o} \rangle / \sigma_*} \left(\mathrm{e}^{\langle \bar{p} \rangle / \sigma_*} - 1 \right) \tag{19}$$

In equation (19), σ_* $\left[ML^{-1}T^{-2}\right]$ is a normalizing stress constant that ranges between 10 and 40 MPa (with low values that correlate with high fracture intensity), k_* $\left[L^2\right]$ is the maximum value of permeability and $\langle \sigma'_{n,o} \rangle = \langle \sigma_n - p_o \rangle$ is the average initial effective normal stress in the fractured cell (with the average total normal stress obtained by projecting the far-field stress tensor onto each fracture plane intersecting the grid cell and then taking the mean value). Note that when the pore-fluid over-pressure $\bar{p}$ is null, $\Delta k = 0$ and the equivalent permeability tensor for the fractured grid-block is given by (15). On the contrary, when $\bar{p} \neq 0$, the increment Δk is applied to the full equivalent permeability tensor, leading to a non-linear pore-fluid propagation in the fractured rock mass.

3.2.2 Stochastic modeling of injection-induced seismicity

We now present the stochastic modeling approach for seismicity nucleation in a fractured rock mass subjected to fluid injection. This approach consists in distributing stochastically weak failure points in the fractured domain, similarly to what has been done in many previous contributions (e.g. Rothert and Shapiro, 2003; Bechmann et al., 2012; Goertz-Allmann and Wiemer, 2013; Gischig and Wiemer, 2013; Rinaldi and Nespoli, 2017; Zbinden et al., 2020; Haagenson and Rajaram, 2021; Karvounis and Wiemer, 2022; Ritz et al., 2022, to cite a few). These weak points represent the center locations of potential seismogenic patches/asperities,

on which seismic deformations may localized if local pore-fluid pressure reaches a critical value. The discrete fracture network in the rock mass, therefore, contributes only to the anisotropic pore-fluid propagation and the conservation of the elastic momentum in the medium is not considered. This is the key characteristic of this *hybrid model* for injection-induced seismicity: the elastic equilibrium of the fractured rock mass, whose resolution is very expensive computationally, is replaced by a stochastic distribution of weak failure points whose activation strictly depends on the (physic-based) spatial-temporal evolution of pore-fluid pressure. Note that these weak failure points are essentially the seeds points previously introduced in the SEED model, i.e. potential locations of earthquakes. Here, however, we refer to them as weak failure points due to their constitutive rupture model that will be presented in the following.

3.2.3 Stress state and weak failure points distribution in the fractured rock mass

Let us consider a fractured rock mass with a set of pre-existing inter-connected fractures/faults in the $\mathbb{R}^3$ Euclidean space with canonical global basis $\hat{\mathbf{e}}_x = (1,0,0)$, $\hat{\mathbf{e}}_y = (0,1,0)$ and $\hat{\mathbf{e}}_z = (0,0,1)$ and reference origin $O = (0,0,0)$. The fracture network can be stochastically generated (i.e. positions, orientations and dimensions can be generated using appropriate probability distributions) or can be obtained from out-crop and/or core testing data. We further assume that each pre-existing fracture f is disk-shaped, with a given radius R^f and hydraulic aperture w_h^f, and is uniquely identified in the Euclidean space by a centre point $C^f = \left(x^f, y^f, z^f\right)$ and an orthonormal vector $\hat{\mathbf{n}}^f$ (with its origin in C^f). The fractured rock mass is subjected to a depth-dependent far-field principal stress state, characterized by a vertical principal component $\sigma_v(z)$ and two horizontal principal components $\sigma_H(z)$ and $\sigma_h(z)$ (with $\sigma_H > \sigma_h$). Their values are typically estimated from deep hydraulic injection tests, with a certain degree of uncertainty that is always present during measurement operations (Cornet and Valette, 1984). In order to take that into account, the principal stress components are sampled from a normal distribution, with a depth average value taken from in-situ stress estimates and a certain standard deviation σ, i.e.

$$\begin{aligned} \langle \sigma_v(z) \rangle &\sim \mathcal{N}\left(\sigma_{v,meas}(z), \sigma\right) \\ \langle \sigma_H(z) \rangle &\sim \mathcal{N}\left(\sigma_{H,meas}(z), \sigma\right) \\ \langle \sigma_h(z) \rangle &\sim \mathcal{N}\left(\sigma_{h,meas}(z), \sigma\right) \end{aligned} \tag{20}$$

The principal stress tensor Σ_p, whose diagonal entries are given by (20), is then projected onto the geographic coordinate system $north - east - down$ (which is assumed to coincide with the coordinate system x, y, z identified by the canonical basis $\{\hat{\mathbf{e}}_x, \hat{\mathbf{e}}_y, \hat{\mathbf{e}}_z\}$ and origin O) via the following linear transformation

$$\Sigma_g = R_{pg}^T \Sigma_p R_{pg}, \tag{21}$$

where

$$R_{pg} = \begin{bmatrix} \cos(\alpha)\cos(\beta) & \sin(\alpha)\cos(\beta) & -\sin(\beta) \\ \cos(\alpha)\sin(\beta)\sin(\gamma) - \sin(\alpha)\cos(\gamma) & \sin(\alpha)\sin(\beta)\sin(\gamma) + \cos(\alpha)\cos(\gamma) & \cos(\beta)\sin(\gamma) \\ \cos(\alpha)\sin(\beta)\cos(\gamma) + \sin(\alpha)\sin(\gamma) & \sin(\alpha)\sin(\beta)\cos(\gamma) - \cos(\alpha)\sin(\gamma) & \cos(\beta)\cos(\gamma) \end{bmatrix}$$

is a rotation matrix that includes the cosines of the director angles α, β and γ (see Zoback (2010) for more details).

Unlike previous contributions where weak failure points are uniformly distributed in the simulation domain, which - in almost all the cases - does not even include pre-existing fractures/faults to account for fluid flow anisotropy (e.g. (Goertz-Allmann et al., 2011; Bechmann et al., 2012; Gischig and Wiemer, 2013; Rinaldi and Nespoli, 2017)), here we distribute the weak points only along the pre-existing fractures in the rock mass (see Figure 8). This is because deformations, if they occur, are expected to be localized along patches of the discrete fracture network and not within the intact rock matrix. A set of weak points per fracture is thus

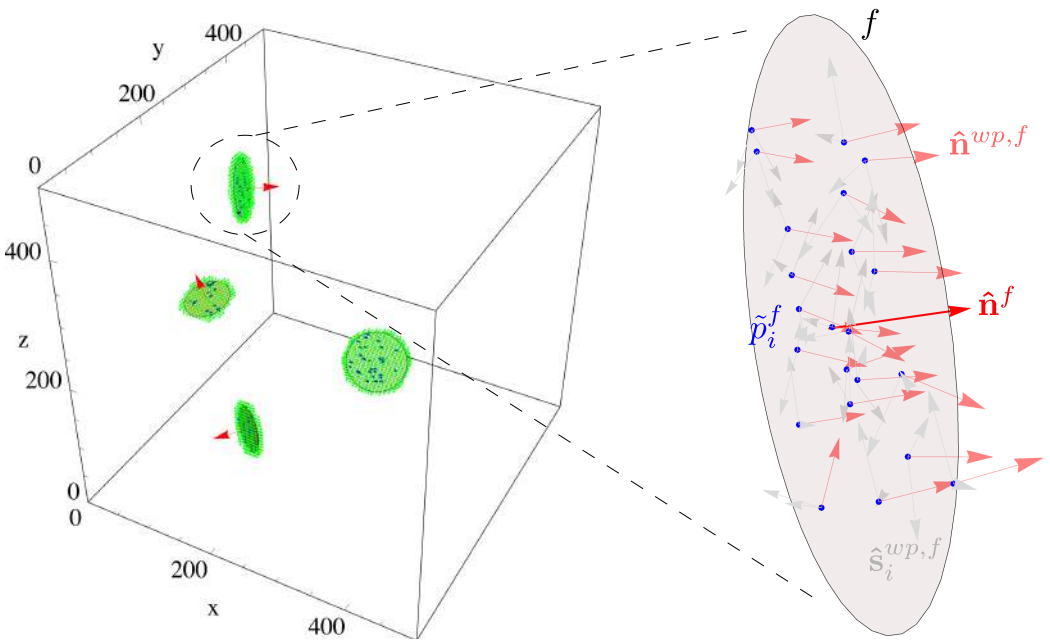

Figure 8: Distribution of weak failure points along pre-existing fractures. Cuboids intersected by the pre-existing fractures are denoted by a green colour. The normal vector of each weak failure point is normally distributed with an average value that is equal to the normal vector of the associated fracture.

sampled from a uniform distribution, such that the total set of discrete weak points Ω_{wp} is given by

$$\Omega_{wp} = \bigcup_{f=1}^{N^f} \Omega_{wp}^f, \tag{22}$$

where N^f is the total number of discrete fractures and Ω_{wp}^f is the set of weak points $\tilde{p}_i$ per fracture

$$\Omega_{wp}^f = \{\tilde{p}_1^f, \tilde{p}_2^f, \tilde{p}_3^f, \dots\} \tag{23}$$

It is worth mentioning that the total number of weak points per fracture may vary, but the density, defined as the number of weak points per volume of fracture, is enforced to be the same. This implies that longer fractures are seeded with more weak points compared to shorter ones.

At each weak point $\tilde{p}_i$ belonging to fracture f, we assign an orthonormal basis $\{\hat{\mathbf{s}}_1^{wp,f}, \hat{\mathbf{s}}_2^{wp,f}, \hat{\mathbf{n}}^{wp,f}\}$ that identifies the patch plane on which the far-field stress tensor Σ_g is projected onto. Since weak points are distributed along pre-existing fractures and represent their potential unstable patches/asperities, the components of the normal vector $\hat{n}_i^{wp,f}$ are sampled from a normal distribution, with average values equal to the components of fracture normal vector $\hat{n}_i^f$, i.e. $\langle \hat{n}_i^{wp,f} \rangle \sim \mathcal{N}\left(\hat{n}_i^f, \bar{\sigma}\right)$ where $\bar{\sigma}$ is the corresponding standard deviation. The plane orientation that crosses point $\tilde{p}_i^f$ is thus similar to the corresponding fracture plane. The two other shear orthonormal vectors, $\hat{\mathbf{s}}_1^{wp,f}$ and $\hat{\mathbf{s}}_2^{wp,f}$, are instead randomly sampled from a uniform distribution and may be oriented in any direction along the plane orthogonal to $\hat{\mathbf{n}}^{wp,f}$.

The stress state on each weak failure points $\tilde{p}_i^f$ is then simply given by

$$\begin{aligned} \sigma_n^{wp,f} &= \hat{n}_i^{wp,f} \cdot \Sigma_{g,ij} \cdot \hat{n}_j^{wp,f} \\ \tau_1^{wp,f} &= \hat{s}_{1,i}^{wp,f} \cdot \Sigma_{g,ij} \cdot \hat{n}_j^{wp,f} \\ \tau_2^{wp,f} &= \hat{s}_{2,i}^{wp,f} \cdot \Sigma_{g,ij} \cdot \hat{n}_j^{wp,f}, \end{aligned} \tag{24}$$

where $\sigma_n^{wp,f}$ is the normal stress component, whereas $\tau_1^{wp,f}$ and $\tau_2^{wp,f}$ are the two shear stress components along $\hat{\mathbf{s}}_1^{wp,f}$ and $\hat{\mathbf{s}}_2^{wp,f}$, respectively. Note that the total shear stress vector reads $\boldsymbol{\tau}^{wp,f} = \tau_1^{wp,f} \cdot \hat{\mathbf{s}}_1^{wp,f} + \tau_2^{wp,f} \cdot \hat{\mathbf{s}}_2^{wp,f}$, and its magnitude can be readily obtained as $\tau^{wp,f} = \left\|\boldsymbol{\tau}^{wp,f}\right\|$. Note also that the first equation in (24) is used to calculate the average total normal stress on a fractured cell in (19) (with $\hat{\mathbf{n}}^{wp,f}$ replaced by

$\hat{\mathbf{n}}^f$).

To our knowledge, this stochasting distribution of stresses and weak failure points is unique of its kind. A similar approach was recently adopted by Haagenson and Rajaram (2021). However, in their approach they do not conceptually consider weak points as centroids of potentially unstable patches, as well as they do not consider stochastic variations of the orthonormal basis associated with each weak failure point. We believe such variations are important since they lead to a heterogeneous distribution of shear strength along adjacent weak points of a pre-existing fracture f, similar to more sophisticated physic-based heterogeneous models for induced seismicity (e.g Almakari et al., 2019; Jin, 2022).

3.2.4 Constitutive relations and rupture model for weak failure points

Upon fluid injection in the naturally fractured rock mass, the local reduction of effective normal stress due to pore fluid pressurization may cause failure/activation of weak points and thus the nucleation of deformations on potentially unstable patches centered on $\tilde{p}_i^f$. The force balance along these patches, however, ensures that the absolute shear stress is equal to the available frictional resistance given by the Mohr-Coulomb yielding criterion

$$\underbrace{\left|\tau^{wp,f}\right| - c - f_c\left(d_s\right) \cdot \left(\sigma_n^{wp,f} - p_o^{wp,f} - \bar{p}^{wp,f}\right)}_{\Delta\tau^{wp,f}} \leq 0, \tag{25}$$

where $p_o^{wp,f}$ and $\bar{p}^{wp,f}$ are the in-situ pore fluid pressure and over-pressure at weak point $\tilde{p}_i^{wp,f}$ respectively, c is the cohesion and f_c is the friction coefficient, which is assumed to weaken linearly and irreversibly with accumulated seismic slip d_s, from a peak f_c^p to a residual f_c^r value over a distance d_c, i.e.

$$f_c = f_c^r + w\left(d_c - d_s\right) H(d_c - d_s) \tag{26}$$

with $w = \left(f_c^p - f_c^r\right)/d_c$ and $H\left(\cdot\right)$ being the friction weakening rate and the Heaviside step function respectively. The local violation of the Mohr-Coulomb criterion (25) leads to localized deformations that may radiate seismic energy due to the weakening nature of friction coefficient. In order to assess whether a failing patch is seismogenic or not, we adopt the following stochastic approach. For each weak failure point that violates (25), we randomly sample a moment magnitude M_w from a truncated Gutenberg-Richter magnitude–frequency law (for a given relative size distribution of earthquakes or $b-$value). To do so, we take advantage of the fact that the G-R law can be transformed into a Pareto distribution for scalar seismic moment M $\left[ML^2T^{-2}\right]$. Hence, we sample a seismic moment from the following truncated Probability Density Function (Kagan, 2002)

$$\phi\left(M\right) = \frac{M_{max}^{\beta} M_{min}^{\beta}}{M_{max}^{\beta} - M_{min}^{\beta}} \beta M^{-1-\beta}, \qquad M_{min} \leq M \leq M_{max} \tag{27}$$

where $\beta = \dfrac{2}{3}b$ (with b being the b-value of the G-R law), and M_{min} and M_{max} are the minimum and maximum seismic moment respectively. We then convert the seismic moment M_o into a moment magnitude M_w using (Hanks and Kanamori, 1979)

$$M_w = \frac{2}{3}\left(\mathrm{Log}_{10}M - 9.05\right) \tag{28}$$

We finally assume that the failing patch centred on $\tilde{p}_i^{wp,f}$ is circular-shaped and calculate the corresponding rupture radius using the following relation (Eshelby, 1957)

$$R^{wp,f} = \sqrt[3]{\frac{7}{16}\frac{M}{\Delta\tau^{wp,f}}} \tag{29}$$

If the rupture radius $R^{wp,f}$ is larger than the characteristic nucleation patch length scale L_c associated with $\tilde{p}_i^{wp,f}$, which is approximately given by (Garagash and Germanovich, 2012)

$$L_c \simeq \frac{G \cdot d_c}{f_c^p \cdot \sigma_{n,o}^{wp,f}} \tag{30}$$

with $\sigma_{n,o}^{wp,f}$ and G being the in-situ effective normal stress at $\tilde{p}_i^{wp,f}$ and shear modulus of the medium respectively, then the failing patch is seismogenic and releases seismic energy. On the contrary, if $R^{wp,f} < L_c$, then the rupture patch is not large enough for the development of an instability and deformations are thus aseismic. For instance, a magnitude $M_w = -1$ leads to a rupture radius of $R^{wp,f} \simeq 2.5$ m for a shear stress drop of $\Delta\tau^{wp,f} = 1$ MPa, which may be larger or lower than L_c that plausibly ranges between $[10^{-1}, 10^{1}]$ m (depending on the value of d_c that may range between $[10^{-4}, 10^{-2}]$ m (Garagash and Germanovich, 2012)). In this rigid-plastic stochastic model, therefore, the violation of the Mohr-Coulomb yielding criterion (25) is a necessary but not sufficient condition for seismicity nucleation. This is in agreement with the fact that deformations that take place at depth upon fluid injection may also be aseismic (hence characterized by not detectable seismic waves), as observed in many in-situ large scale injection campaigns (Bourouis and Bernard, 2007; Scotti and Cornet, 1994) and recent field and laboratory experiments (Guglielmini et al., 2015; Scuderi and Collettini, 2016). Although in this contribution we do not model aseismic slip, we differentiate between seismic and aseismic deformations for two main reasons: first, the relations (28-29) are only valid for seismic sources, and second the assumption that all the triggered deformations radiate seismic energy is too far-fetched.

For a seismogenic patch, the increment of slip associated with a constant stress drop $\Delta\tau^{wp,f}$ on a circular area $A^{wp,f} = \pi \left(R^{wp,f}\right)^2$ can be readily obtained from Aki K. (1966) as

$$\Delta d_s = \frac{M}{G A^{wp,f}}, \tag{31}$$

with the slip direction that is equal to the direction of the applied shear stress, i.e. $\hat{\boldsymbol{\tau}}^{wp,f} = \dfrac{\boldsymbol{\tau}^{wp,f}}{\|\boldsymbol{\tau}^{wp,f}\|}$, and the associated friction coefficient drop obtained from (26). Assuming further a non-associative plastic flow rule similar to the one proposed by Ciardo and Lecampion (2019), we can express an increment of opening associated with shear-induced dilatancy as

$$\Delta d_n = \Delta d_s \cdot \tan(\Psi), \tag{32}$$

where Ψ is a dilatant angle. A seismogenic weak point/patch is thus characterized by a dislocation vector $\boldsymbol{\Delta d} = \{\Delta d_{s_1}, \Delta d_{s_2}, \Delta d_n\}$, where the three local components can be readily obtained as follow

$$\begin{aligned} \Delta d_{s_1} &= \left\| \left(\Delta d_s \cdot \hat{\boldsymbol{\tau}}^{wp,f} \right) \cdot \hat{\mathbf{s}}_1^{wp,f} \right\| \\ \Delta d_{s_2} &= \left\| \left(\Delta d_s \cdot \hat{\boldsymbol{\tau}}^{wp,f} \right) \cdot \hat{\mathbf{s}}_2^{wp,f} \right\| \\ \Delta d_n &= \left\| \Delta d_n \cdot \hat{\mathbf{n}}^{wp,f} \right\| \end{aligned} \tag{33}$$

Such dislocations alter the stress state in the fractured rock mass, potentially triggering other weak patches. In the following section, we describe how the active seismic sources transfer elastic stresses in the medium, together with a re-triggering mechanism for seismic repeaters.

3.2.5 Elastic stress interactions and re-triggering mechanism for partial ruptures

Several studies have shown that earthquakes interaction is an important mechanism in induced-seismicity (e.g. (King et al., 1994; Lin and Stein, 2004)), even when the majority of the triggered events are characterised by relatively small magnitudes (Brown and Ge, 2018). In this contribution we assume that, when the local stress state on a generic weak failure point violates the Mohr-Coulomb yielding criterion and the resulting failure patch is seismogenic, a source of elastic stress changes is considered. Notably, we assume that a source seismic patch transfers elastic stress changes on all the others weak points in a quasi-static manner. When multiple seismogenic patches are activated, multiple concurrent sources are considered.

Unlike previous works in which stress interactions are calculated using Okada, Y. (1992)'s analytical solutions of a finite rectangular dislocation in a homogeneous, isotropic and linear elastic half-space (e.g. King et al., 1994; Toda et al., 1998; Lin and Stein, 2004; Catalli et al., 2013, to cite a few), here we use the analytical elastic solutions of a constant strength dislocation over a finite rectangular patch in an unbounded

elastic medium (Shou et al., 1997). The effect of the free-surface is thus not taken into account, implying that the modeling domain must be at sufficiently large depths where the effect of the traction free surface becomes negligible.

Assuming to have N^s seismogenic weak failure points that we denote as $\tilde{p}_i^{f,s}$ (such that $\Omega_{wp}^s \subset \Omega_{wp}$), in view of problem linearity the increment of tractions on a generic weak failure point $\tilde{p}_j^f$ can be obtained as

$$\Delta \mathbf{t}_j = \sum_{i=1}^{N^s} \mathbf{E}_l^{ji} \cdot \Delta \mathbf{d}_i, \tag{34}$$

where $\Delta \mathbf{t}_j = \{\Delta\tau_1, \Delta\tau_2, \Delta\sigma_n\}$ is the vector of increment of tractions along the local orthonormal basis of the receiver point and $\mathbf{E}_l^{ji}$ the local elastic influence matrix that map the effects of source weak point i onto receiver point j (see (Shou et al., 1997) for more details). Note that the seismogenic source patch is circular, whereas the analytical elastic stress kernels used to evaluate the entries of $\mathbf{E}_l^{ij}$ are built on a rectangular finite patch. In this contribution, therefore, the kernels are evaluated over a squared area, albeit this is an approximation.

By applying equation (34) for all the weak failure points distributed in the elastic medium, we can calculate all the mutual effects of quasi-static deformations. We believe that these quasi-static effects are very important since they may drive the spatial-temporal evolution of seismicity in critically stressed fractured reservoirs, as discussed in (Ciardo et al., 2020).

Another important mechanism that is not often consistently modeled in other similar and stochastic hybrid models is the re-triggering of weak points. Some approaches assume that once a weak failure point is activated and release seismic energy, it can not be re-activated again and hence is discarded (e.g. (Karvounis and Wiemer, 2022)). In other approaches, instead, a failure weak point can be theoretically activated infinite times, as long as the over-pressure is critical enough to locally violate the Mohr-Coulomb criterion (25) in that point (e.g. Catalli et al., 2016; Rinaldi and Nespoli, 2017; Ritz et al., 2022). This tacitly assumes that the friction coefficient is instantaneously recovered after each triggered seismic event, or that the weakening of friction coefficient occurs over an infinite length scale. Here, instead, we adopt a different approach that is consistent with the physic-based constitutive relations that we have assumed to be valid for each weak failure point/patch in the medium (see Section 3.2.4). Namely, we suppose that each weak failure point/patch $\tilde{p}_i^{wp,f}$ can potentially host multiple seismic events as long as the accumulated seismic slip d_s is lower than the slip weakening scale d_c. Thus, on each weak point we keep track of the accumulated seismic slip (if any) at the time scale of injection: if it is lower than d_c, the friction coefficient has not reached its residual value and seismic ruptures are potentially allowed to (re)-nucleate (if the conditions described above are satisfied). On the other hand, if the accumulated slip is larger than d_c, the shear strength of the failing patch is at its residual value and can not be recovered due to the irreversibility of friction coefficient with slip. Hence, in this case the weak failure point is discarded (although it may still contribute to aseismic deformations, here not considered). This simple approach allows the potential nucleation of multiple partial seismic ruptures on a same failure patch, which is a scenario that may occur when micro-seismic events are triggered over a large rupture patch. Finally, it is worth mentioning that this condition for triggering partial ruptures allows also a physically consistent treatment of the dilatant behaviour of the seismogenic patches, for which a critical state is expected to be reached when the slip is larger than d_c (see Figure 2 in Ciardo and Lecampion (2019) for instance).

3.2.6 Numerics

The modeling approach presented in previous sections consists of two parts that are coupled between each other via the principle of effective normal stresses. For a given pore-fluid pressure field, a stochastic distribution of potential seismic events and deformations can be obtained from the local evaluation of the Mohr-Coulomb yielding criterion (25) on each weak failure point. These plastic deformations, however, do not affect pore-fluid pressure evolution, leading to a one-way coupling between fluid flow and deformations. Note that only the transient problem of pore-fluid flow propagation in the fractured medium (13-19) requires

a numerical resolution. The stochastic forecast of seismicity instead is obtained upon analytical evaluations (25-34) (included the quasi-static elastic stress interactions).

In this contribution, we adopt a Finite Volume scheme with Multi-Point Flux Approximation (Aavatsmark, 2002) for the spatial discretization of fluid fluxes in the equivalent continuum medium, which is obtained upon mapping all the pre-existing fractures in the computational grid (see example in Figure 8). We choose this numerical method due to its capability to discretize correctly the fluid flow equations for general nonorthogonal grids and for general orientation of the principal directions of the permeability tensor (Aavatsmark, 2002). As stated beforehand, being able to properly capture flow anisotropy in our continuum equivalent approach is crucial for reproducing the real percolation behaviour of the discrete fracture network. When a pre-existing fracture is mapped onto the computational grid and is not aligned with grid directions (like in the example reported in Figure 8), the principal directions of the permeability tensor are also misaligned and the resulting equivalent permeability tensor (15) is dense and anisotropic. A classic Finite Volume scheme with Two-Point Flux Approximation would not be able to solve accurately such anisotropic behaviour, but it would actually lead to a stair-like pore-fluid flow propagation and hence an accumulation of error in the fluxes computation, as demonstrated in many previous works (Lee et al., 2002b; Botros et al., 2008; Rutqvist et al., 2013).

We have implemented the numerical scheme for non-linear pore-fluid propagation in the fractured medium and stochastic forecast of seismicity previously described in Wolfram Mathematica (Wolfram Research, Inc., 2022). In order to speed up computations, we have exposed part of the code to C++ via LTemplate, which is an open-source Wolfram package that simplifies the usage of LibraryLink C/C++ API (see source code at `https://github.com/szhorvat/LTemplate`). In particular, we have exposed only the operations with computational complexity of $\mathcal{O}(m \cdot n)$, where n and m are two variables that can both be very large. These operations are:

- Mapping of all the pre-existing fractures onto the computational mesh. This method consists in a double nested loop (the outer over all the pre-existing fractures and the inner over all the mesh finite elements) that flags the mesh elements intersected by each pre-exisiting fracture. For a given element intersected by a fracture, the algorithm returns the corresponding element index and the associated fracture index (both integers).

- Evaluation of elastic stress interactions. This method also involves a double nested loop, with the outer loop over all the seismogenic weak points Ω^s_{wp} and the inner one over all the weak points Ω_{wp}. When the number of seismic events gets large, the calculations of the mutual elastic stress interactions might get slower. With the usage of LTemplate, an order of magnitude of speed-up is obtained circa.

- Assembling of the Multi-Point Flux Approximation matrix. Although the computational complexity of the method that assembles such a $N^e \times N^e$ sparse matrix is $\mathcal{O}(r \cdot N^e)$, with r being a small scalar value, its call is performed at every fixed-point iteration (due to the non-linear variations of fractured permeability tensors with local effective normal stress) and every loading (time) increment.

3.2.7 Verification of flow numerical solver

We benchmarked the numerical solver for pore-fluid propagation in porous media previously presented against some analytical and numerical solutions. This is a common practice in the community of fluid flow in porous media (e.g. (Flemisch et al., 2018)).

For sake of space, we report only one verification test, which corresponds to the case of an instantaneous point source injection in an anisotropic unfractured porous medium. For this test, we consider a simulation domain of $11 \times 11 \times 11$ m, uniformly discretized with cuboids of $0.11 \times 0.11 \times 0.11$ m (the total number of finite elements is 10^6). A fluid mass $\Delta Q = 0.01$ Kg of water is instantaneously released in a point ($x_{inj} = 5.555, y_{inj} = 5.555, z_{inj} = 5.555$) of the homogeneous medium. In this test, we assume the the principal directions of the permeability tensor are aligned with the grid directions, but anisotropic conditions between $x-$, $y-$ and $z-$directions are considered. Notably, we assume that the permeability along $x-$direction is larger than the permeability along $y-$direction, which in turn is larger that the permeability

Table 2: Input parameters for verification test.

Symbol	Description	Value
Fluid and material properties		
ρ	Fluid density	10^3 $\left[\mathrm{Kg/m^3}\right]$
β	Compressibility parameter	10^{-10} [1/Pa]
μ	Fluid kinematic viscosity	10^{-3} [Pa $\cdot$ s]
ϕ	Porosity	10^{-2} [–]
Permeability tensor properties		
k_{xx}	Permeability	10^{-15} $\left[\mathrm{m^2}\right]$
k_{yy}	Permeability	$0.5 \cdot 10^{-15}$ $\left[\mathrm{m^2}\right]$
k_{zz}	Permeability	10^{-16} $\left[\mathrm{m^2}\right]$
$k_{xy} = k_{yz} = k_{xz}$	Permeability	0. $\left[\mathrm{m^2}\right]$
In-situ conditions		
p_o	Uniform pore fluid pressure	10^7 [Pa]
Injection parameters		
ΔQ	Mass	0.01 [Kg]
$(x_{inj}, y_{inj}, z_{inj})$	Injection location	$(5.555, 5.555, 5.555)$ [m]
Simulation parameters		
t_{init}	Initial time	0. [s]
t_{end}	End time	2. [s]
Δt	Time step	0.01 [s]
t_s	Time of instantaneous release	0.01 [s]

in $z-$direction (see their values in summary Table 2). Pore-fluid over-pressure is thus expected to dissipate faster along the x-direction compared to the other two.

For this specific problem, there exists also an analytical solution that reads (Carslaw and Jaeger, 1959)

$$p\left(x,y,z,t\right) - p_o = \frac{\left(\Delta Q/\left(\rho\beta\right)\right)\left(\mu\beta\right)^{3/2}}{8\left(\pi^3\left(t-t_s\right)^3 k_{xx}k_{yy}k_{zz}\right)^{1/2}} \cdot \mathrm{Exp}\left(\frac{-\mu\phi\beta}{4\left(t-t_s\right)}\left(\frac{\left(x-x_{inj}\right)^2}{k_{xx}} + \frac{\left(y-y_{inj}\right)^2}{k_{yy}} + \frac{\left(z-z_{inj}\right)^2}{k_{zz}}\right)\right) \tag{35}$$

where t_s is the specific time at which the fluid mass ΔQ is released in the homogeneous and anisotropic porous medium. Assuming an initial uniform pore pressure distribution $p_o = 10$ MPa and no-flux boundary conditions, we solve numerically the corresponding time-dependent boundary value problem using the parameters reported in Table 2. The left and top-right plots in Figure 9 show the spatial profiles of pore-fluid over-pressure for different time snapshots, along three orthogonal directions crossing the injection point. We can readily observe that, for each time snapshot, the spatial extent of fluid over-pressure is much larger along x-direction, compared to the others (as expected). Furthermore, a good match between numerical and analytical solution is obtained. Although at early time there is a bit of discrepancy between numerical and analytical solutions in a small region near injection point (along all the directions), the numerical solution quickly catches up with the analytical one. At time $t = 1.9$ s the corresponding relative errors (reported in bottom-right plot) are everywhere lower than 5% (on distances where the over-pressure is not null).

3.2.8 Application to FORGE 2022 stimulation: preliminary results

We present now preliminary results related to the FORGE 16A stimulation of April 2022. We generated stochastically a Discrete Fracture Network representative of the FORGE Test site in-situ conditions. Using the available data (Utah FORGE - University of Utah, 2022), we generated 25500 pre-existing disk-shaped fractures uniformly distributed in the computational domain (see Figure 10-a). Fracture radii follow a Pareto distribution with minimum radius of $R_{min} = 10$ m and a power law exponent of $a = 3.2$ (as suggested by outcrop data (Utah FORGE - University of Utah, 2022)); fracture apertures are related to fracture radii via a sub-linear power law (Utah FORGE - University of Utah, 2022) (with power law exponent of 0.5) and finally

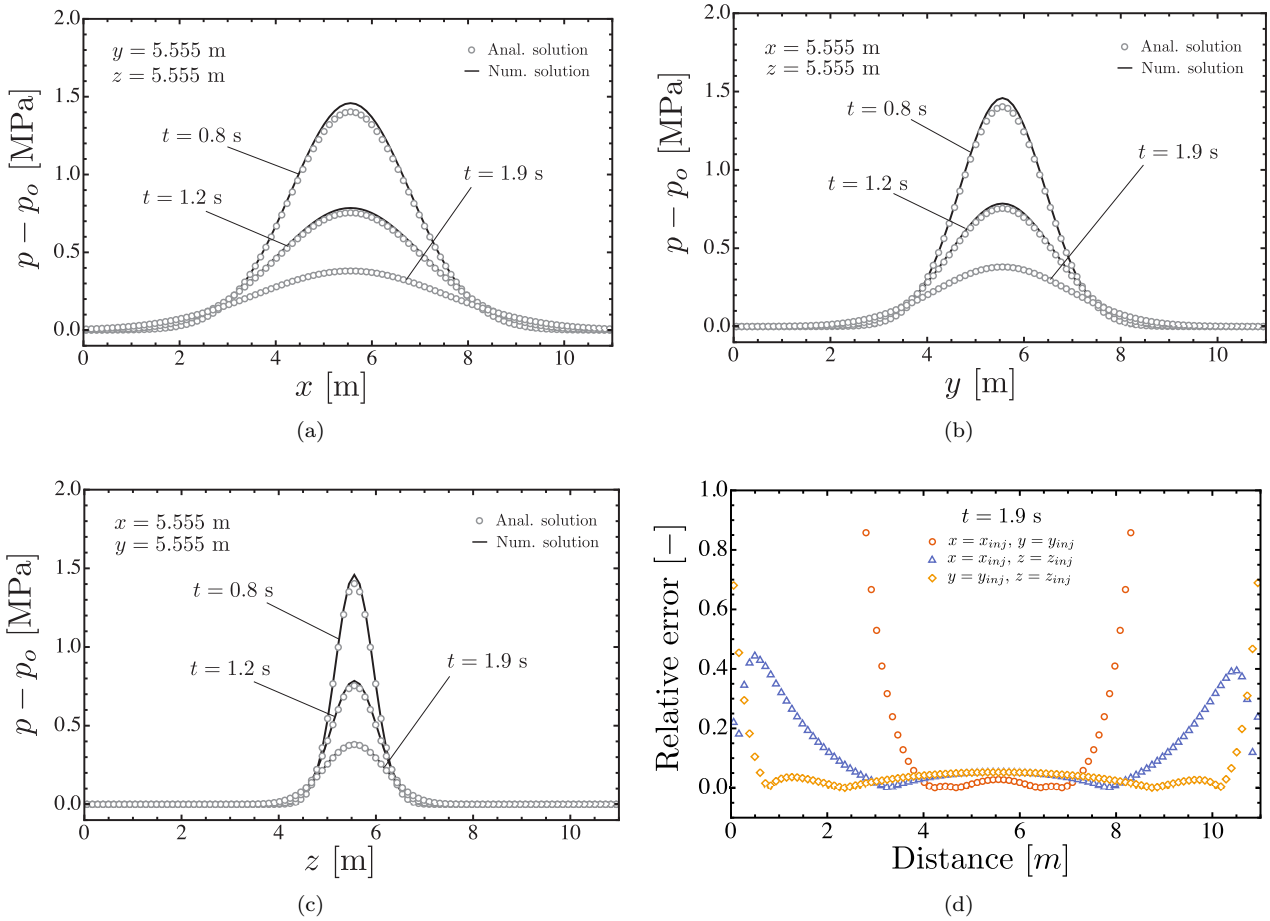

Figure 9: Benchmark of fluid-flow solver against the analytical solution for instantaneous point source injection in an anisotropic unfractured porous medium. Panels (a), (b) and (c) show time snapshots in terms of pore-fluid over-pressure $p - p_o$ along three orthogonal directions crossing the injection point. Panel (d) shows the corresponding relative error.

strike and dip angles follow a Fisher distribution with a mean angle and a concentration factor (see (Utah FORGE - University of Utah, 2022) for all the input data for fractures generation).

The fractured rock mass is subjected to an in-situ uniform pore-fluid pressure $p_o = 24.6$ MPa and a normal stress regime, with a vertical principal stress $\sigma_v = 64.9$ MPa, and two horizontal principal stresses of $\sigma_H = 54.0$ MPa and $\sigma_h = 43.1$ MPa (with a direction of σ_H of $N25°E$ - see Figure 10-a). The standard deviation associated with each principal stress is respectively 0.05, 0.2 and 0.1. We distributed along the pre-existing frictional fractures, characterised by a friction coefficient $f = \text{Tan}(37°)$ and a dilatant angle $\Psi = 2°$, 95730 weak failure points (with a density of points per fracture of ∼1000). The effective stress state associated with each weak failure point is reported in Figure 10-d.

Fluid is injected in the middle of the computational domain (see Figure 10-b), following the strategy reported in panel 10-c. Note that we adopted a fluid viscosity of $\mu = 10^{-1}$ Pa·s that is approximately similar to the viscosity of the fluid adopted during the real injection experiment (power law rheology).

Upon mapping all the pre-existing fractures onto the computational domain composed of 1 millions of regular cuboids (see Figure 10-b), we generated the equivalent properties of the single continuum medium. Namely, we generated the equivalent permeability field and the equivalent porosity field, as displayed in Figure 11. We then ran a forward simulation in order to forecast seismicity.

Figure 12 shows the generated seismicity cloud for different viewpoints at the end of the numerical experiment. The total number of events triggered by anisotropic pore-fluid migration from injection point is 3994, with a maximum moment magnitude of 0.96. It is interesting to note that seismicity spread away from injection point consistently with in-situ critical stress directions. The blue dashed lines reported in Figure 12, which identify the directions associated with the critical orientations $\theta_c = \pm(\pi/4 + \text{ArcTan}(f)/2) = 82°$,

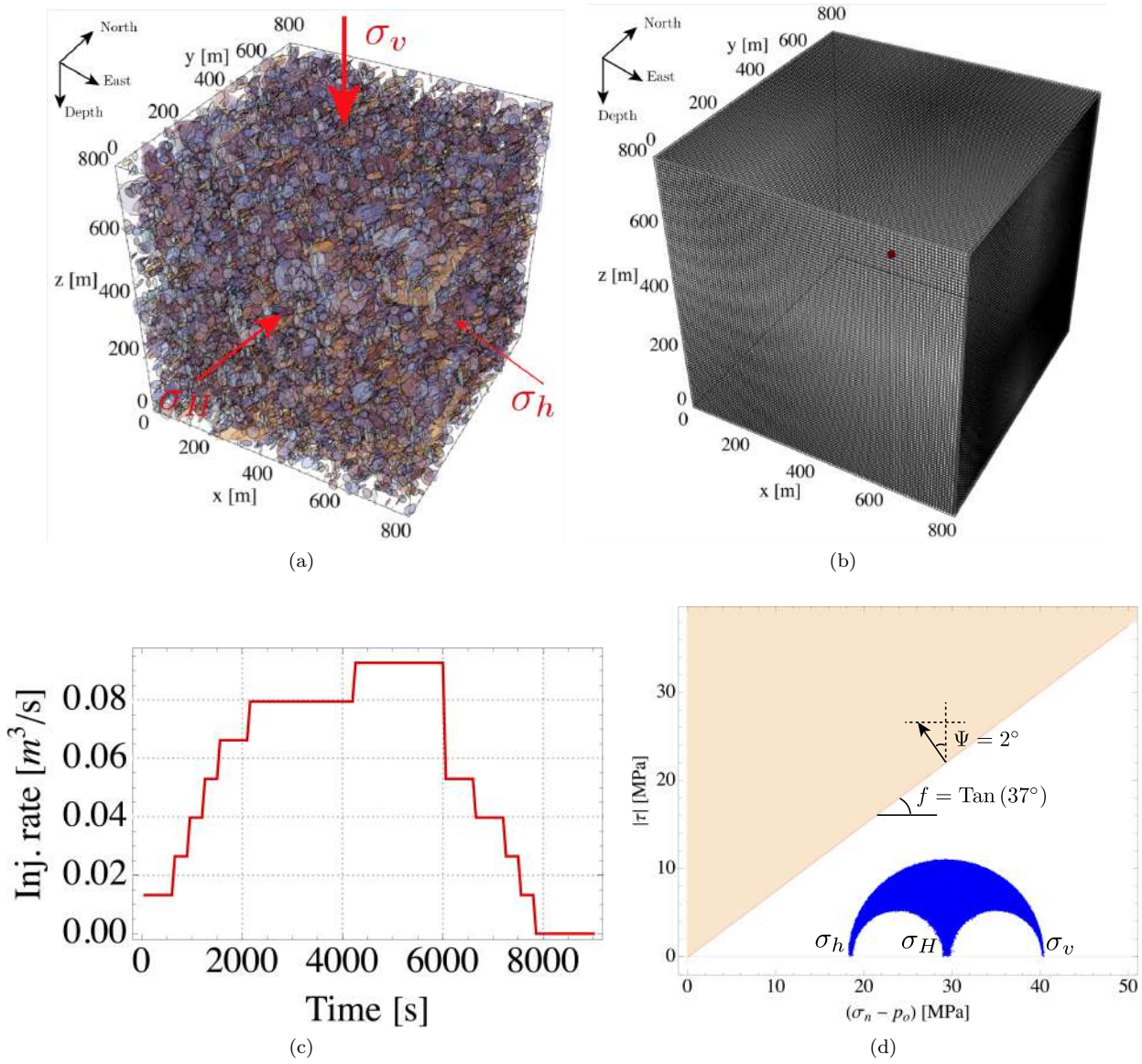

Figure 10: Panel (a): stochastic Discrete Fracture Network generated using an ad-hoc developed algorithm. Radii, strike and dip angles of each fractures are sampled from given distributions to resemble in-situ condition at FORGE test site. Panel (b): Simulation box of 800 × 800 × 800 meters, centred on injection point (red point) located at 2.536 km depth. This simulation box is discretized with a structured mesh composed of 1 million of cuboids, resulting in 1030301 mesh nodes. Panel (c): Injection protocol adopted. Panel (d): Distribution of fractures' effective stress states on the Mohr-Coulomb plot.

are aligned with seismicity strands. The temporal evolution of induced-seismicity suggests also that part of the events are triggered by elastic stress interactions.

4 Future directions

Hybrid models have the potential to become important components for induced seismicity mitigation strategies. They provide a more accurate description of key physical processes than pure statistical models, still being fast enough for real-time or pseudo-real time applications.

In this deliverable, we have presented a new suite of hybrid hydro-mechanical models for induced seismicity forecasting. HM0 and HM1 models are uni-dimensional hybrid models and thus can efficiently be used to forecast seismicity in real-time or pseudo real-time. An inverse capability based on Differential Evolution algorithm has been implemented and tested successfully with BedrettoLab and FORGE datasets. Notably, the results associated with the hydraulic stimulation at the BULGG show that HM1-SEED is the model that performs the best (compared to the others - see Figure 5), whereas HM0-CAPS is the one that has

t!]

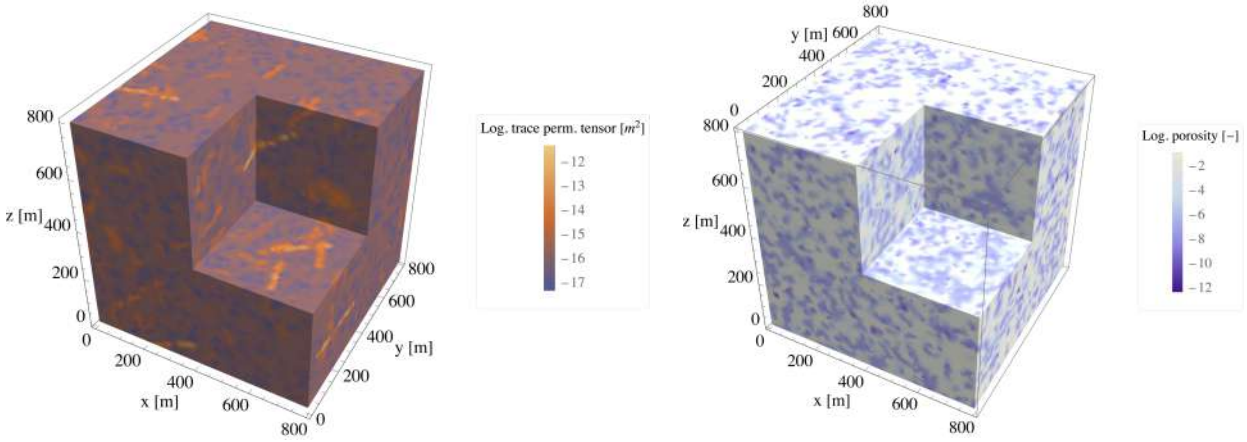

(a) (b)

Figure 11: Equivalent continuum models obtained upon mapping all the pre-existing fractures onto the computational domain. Panel (a) represents the equivalent permeability field, whereas panel (b) represents the equivalent porosity field prior to fluid injection.

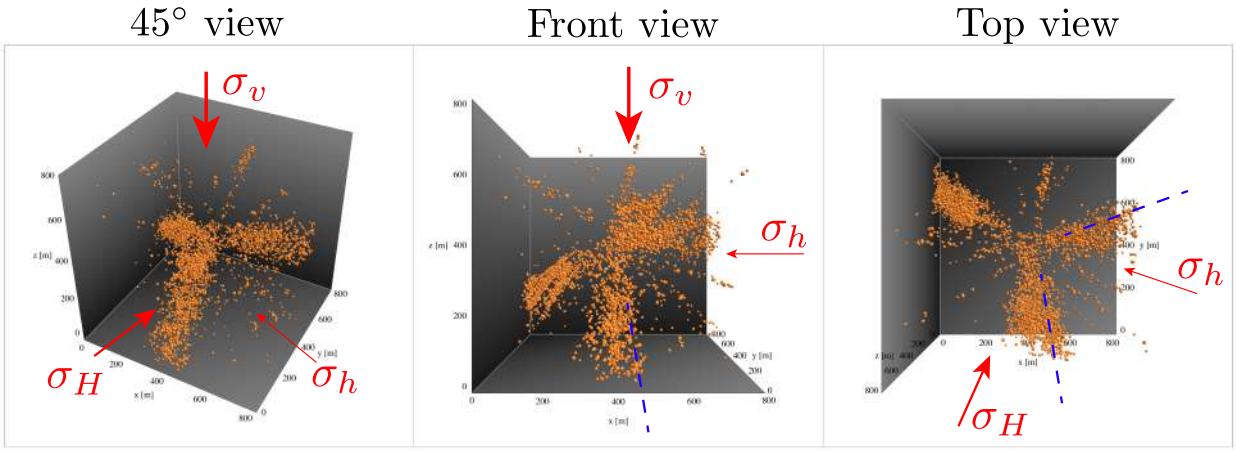

(a)

Figure 12: Different view angles showing micro-seismicity cloud generated with HMStat. Blue dashed lines represent the critical directions, i.e. the directions associated with the critical orientations $\theta_c = \pm(\pi/4 + \text{ArcTan}(f)/2) = 82°$.

the worst performance. Although they are very promising due to their low computational cost, they can be further improved. Spatial distribution of seismicity and magnitudes, for instance, can also be included in the inverse modeling procedure, leading to a more physically consistent calibration of model parameters. In the future, we plan to implement the aforementioned features and further test these models using more datasets. Furthermore, we will test the real-time applicability of these models by running them in a pseudo-perspective way introducing a data assimilation scheme. The presented hybrid models will be used together with state-of-the-art statistical models (see D3.1) to assess the pseudo-real time seismicity forecasting performances in the test-bench exercise foreseen within the activity of WP3 as reported in the Mid-term evalution report.

As far as HMStat is concerned, we have presented a new three-dimensional hybrid model that accounts for non-linear pore-fluid propagation in fractured rock masses. We have introduced substantial improvements compared to similar existing models. Namely, we now account for a frictional weakening constitutive relation for the weak failure points and a criterion that allows to differentiate between seismic and aseismic slip, as well as seismic repeaters. Obviously, this model is more computationally expensive than HM0/1 due to its 3D nature. Nevertheless, it can be potentially used for pseudo-real time applications, since we plan to implement the current model with an inversion scheme. In the current version of this hybrid model, the calibration of parameters must be done manually and thus the applicability of this model reduces to only a forward

forecasting of seismicity, that indeed is essential to build up physics based synthetic catalogs of seismicity to be used in a scenario-based hazard and risk evaluation.

In the future, the release of an upgraded and revised seismicity catalog of the FORGE 2022 stimulation will allow us to improve the forward capabilities of HMStat. To this end, more simulations and realizations will be performed in order to properly investigate the stochasticity of the model and compared the results with observations. We will finally replace the stochastic discrete fracture network with the one provided by the FORGE team and available on `https://gdr.openei.org` to better tailor the model's outcome to the FORGE test site.

Bibliography

F. Grigoli, S. Cesca, E. Priolo, A. P. Rinaldi, J. F. Clinton, T. A. Stabile, B. Dost, M. Garcia Fernandez, S. Wiemer, T. Dahm Current challenges in monitoring, discrimination and management of induced seismicity related to underground industrial activities: an European perspective. *Review of Geophysics*, 55, 310-340.

J. H. Healy, W. W. Rubey, D. T. Griggs, and C. B. Raleigh. The Denver Earthquakes. *Science*, 161(3848): 1301–1310, 1968.

W. L. Ellsworth. Injection-induced earthquakes. *Science*, 341, July 2013.

M.D. Zoback and H.-P. Harjes. Injection-induced earthquakes and crustal stress at 9 km depth at the KTB deep drilling site, Germany. *Journal of Geophysical Research: Solid Earth*, 102(B8):18477–18491, 1997.

N. Deichmann and D. Giardini. Earthquakes Induced by the Stimulation of an Enhanced Geothermal System below Basel (Switzerland). *Seismological Research Letters*, 80(5):784–798, 2009.

F. Grigoli, S. Cesca, A. P. Rinaldi, A. Manconi, J. A. López-Comino, J. F. Clinton, R. Westaway, C. Cauzzi, T. Dahm, S. Wiemer The November 2017 Mw 5.5 Pohang earthquake: A possible case of induced seismicity in South Korea. *Science*, 360, 1003-1006.

A. Mignan, M. Broccardo, and D. Giardini. Induced seismicity closed-form traffic light system for actuarial decision-making during deep fluid injections. *Nature - Scientific reports*, 7, 2017.

C. E. Bechmann, S. Wiemer, B. P. Goertz-Allmann, and J. Woessner. Influence of pore-pressure on the event-size distribution of induced earthquakes. *Geophysical Research Letters*, 39(L09302), 2012.

Valentin S Gischig and Stefan Wiemer. A stochastic model for induced seismicity based on non-linear pressure diffusion and irreversible permeability enhancement. *Geophysical Journal International*, 194(2):1229–1249, 2013.

B. P. Goertz-Allmann and S. Wiemer. Geomechanical modeling of induced seismicity source parameters and implications for seismic hazard assessment. *Geophysics*, 78(1):KS25–KS39, 2013.

A. P. Rinaldi and M. Nespoli. TOUGH2-seed: A coupled fluid flow and mechanical-stochastic approach to model injection-induced seismicity. *Computers & Geosciences*, 108:86–97, 2017.

D. Zbinden, A. P. Rinaldi, T. Diehl, S. Wiemer. Potential influence of overpressurized gas on the induced seismicity in the St. Gallen deep geothermal project (Switzerland). *Solid Earth*, 11:909–933, 2020.

D. Karvounis and S. Wiemer. A discrete fracture hybrid model for forecasting diffusion-induced seismicity and power generation in enhanced geothermal systems. *Geophysical Journal International*, 230(1):84–113, 2022.

V. Ritz, A. P. Rinaldi, and S. Wiemer. Transient evolution of the relative size distribution of earthquakes as a risk indicator for induced seismicity. *Communications Earth & Environment*, 3(249), 2022.

N. Barton, S. Bandis, and K. Bakhtar. Strength, Deformation and Conductivity Coupling of Rock Joints. *Int. J. Rock. Mech. Min. Sci. & Geomech. Abstr.*, 22(3):121–140, 1985.

R. Storn and K. Price. Differential evolution - a simple and efficient heuristic for global optimization over continuous spaces. *Journal of Global Optimization*, 11:341–359, 1997.

J. D. Zechar, M. C. Gerstenberger, and D. A. Rhoades. Likelihood-based tests for evaluating space-rate-magnitude earthquake forecasts. *Bulletin of the Seismological Society of America*, 100(3):1184–1195, 2010. ISSN 00371106. doi: 10.1785/0120090192.

Y. Y. Kagan and D. D. Jackson. New seismic gap hypothesis: five years after. *Journal of Geophysical Research*, 100(B3):3943–3959, 1995. ISSN 01480227. doi: 10.1029/94JB03014.

Y. Y. Kagan and L. Knopoff. Statistical short-term earthquake prediction. *Science*, 236:1563–1567, 1987. doi: doi:10.1126/science.236.4808.1563.

L. Passarelli, L. Sandri, and A. Bonazzi. Bayesian hierarchical time predictable model for eruption ocurrence: an application to kilauea volcano. *Geophysical Journal International*, 181:1525–1538, 2010. doi: 10.1111/j.1365-246X.2010.04582.x.

H. S. Carslaw and J. C. Jaeger. *Conduction of heat in solids.* Oxford Univ Press, 1959.

J. C. S. Long, J. S. Remer, C. R. Wilson, and P. A. Witherspoon. Porous media equivalents for networks of discontinuous fractures. *Water Resources Research*, 18(3):645–658, 1982.

I. Berre, F. Doster, and E. Keilegavlen. Flow in fractured porous media: A review of conceptual models and discretization approaches. *Transport in Porous Media*, 130:215–235, 2019.

C. P. Jackson, A. R. Hoch, and S. Todman. Self-consistency of a heterogeneous continuum porous medium representation of a fractured medium. *Water Resources Research*, 36(1):189–202, 2000.

U. Svensson. A continuum representation of fracture networks. part i: Method and basic test cases. *Journal of Hydrology*, 250:170–186, 2001.

C. T. O. Leung, A. R. Hoch, and R. W. Zimmerman. Comparison of discrete fracture network and equivalent continuum simulations of fluid flow through two-dimensional fracture networks for the DECOVALEX-2011 project. *Mineralogical Magazine*, 76(8):3179–3190, 2012.

T. Hadgu, S. Karra, E. Kalinina, N. Makedonska, J. D. Hyman, K. Klise, H. S. Viswanathan, and Y. Wang. A comparative study of discrete fracture network and equivalent continuum models for simulating flow and transport in the far field of a hypotethetical nuclear waste repository in crystalline host rock. *Journal of Hydrology*, 553:59–70, 2017.

M. Sweeney, C. W. Gable, S. Karra, P. H. Stauffer, R. J. Pawar, and J. D. Hyman. Upscaled discrete fracture matrix model (UDFM): an octree-refined continuum representation of fractured porous media. *Computational Geosciences*, 24:293–310, 2020.

M. O. Kottwitz, A. A. Popov, S. Abe, and B. J. P. Kaus. Equivalent continuum-based upscaling of flow in discrete fracture networks: the fracture-and-pipe model. *Solid Earth*, 2021.

L. J. Durlofsky. Numerical calculation of equivalent grid block permeability tensors for heterogeneous porous media. *Water resources research*, 27(5):699–708, 1991.

T. Samardzioska and V. Popov. Numerical comparison of the equivalent continuum, non-homogeneous and dual porosity models for flow and transport in fractured porous media. *Advances in Water Resources*, 28: 235–255, 2005.

F. E. Botros, A. E. Hassan, D. M. Reeves, and G. Pohll. On mapping fracture networks onto continuum. *Water Resources Research*, 44(W08435), 2008.

D. Reeves, D. A. Benson, and M. M. Meerschaert. Transport of conservatives solutes in simulated fracture networks: 1. synthetic data generation. *Water Resources Research*, 44(W05404), 2008.

J. Rutqvist, C. Leung, A. Hoch, Y. Wang, and Z. Wang. Linked multicontinuum and crack tensor approach for modeling of coupled geomechanics, fluid flow and transport in fractured rock. *Journal of Rock Mechanics and Geotechnical Engineering*, 5:18–31, 2013.

T. Chen, C. Clauser, G. Marquart, K. Willbrand, and D. Mottaghy. A new upscaling method for fractured porous media. *Advances in Water Resources*, 80:60–68, 2015.

Q. Gan and D. Elsworth. A continuum model for coupled stress and fluid flow in discrete fracture networks. *Geomech. Geophys. Geo-energ. Geo-resour.*, 2:43–61, 2016.

S. H. Lee, H. A. Tchelepi, P. Jenny, and L. J. DeChant. Implementation of a flux-continuous finite-difference method for stratigraphy, hexaedron grids. *SPE Journal*, 2002a.

M. Oda. An equivalent continuum model for coupled stress and fluid flow analysis in jointed rock masses. *Water Resources Research*, 22(13):1845–1856, 1986.

M. Chen, M. Bai, and J.-C. Roegiers. Permeability tensors of anisotrpoic fracture networks. *Mathematical Geology*, 31(4), 1999.

W. F. Brace. A note on permeability changes in geological material due to stress. *Pageoph*, 116, 1978.

W. F. Brace. Permeability of crystalline and argillaceous rocks. *Int. J. Rock Mech. Min. Sci.*, 17:241–251, 1980.

E. Huenges and G. Will. Permability, bulk modulus and complex resistivity in crystalline rocks. In D. Bridgwater, editor, *Fluid movements - element transport and the composition of the deep crust*. 1989.

J. R. Rice. Fault stress states, pore pressure distributions, and the weakeness of the san andreas fault. *International Geophysics*, 51(Fault Mechanics and Transport Properties of Rock: A Festschrift in Honor of W. F. Brace):475–503, 1992.

E. Rothert and S. A. Shapiro. Microseismic monitoring of borehole fluid injections: data modeling and inversion for hydraulic properties of rocks. *Geophysics*, 68(2):685–689, 2003.

R. Haagenson and H. Rajaram. Seismic diffusivity and the influence of heterogeneity on injection-induced seismicity. *Journal of Geophysical Research: Solid Earth*, 126(e2021JB021768), 2021.

FH Cornet and Bernard Valette. In situ stress determination from hydraulic injection test data. *Journal of Geophysical Research: Solid Earth*, 89(B13):11527–11537, 1984.

Mark D Zoback. *Reservoir geomechanics*. Cambridge University Press, 2010.

B. P. Goertz-Allmann, A. Goertz, and S. Wiemer. Stress drop variations of induced earthquakes at the Basel geothermal site. *Geophysical Research Letters*, 38, 2011.

M. Almakari, P. Dublanchet, Hervé, E., and F. Pellet. Effect of the injection scenario on the rate and magnitude content of injection-induced seismicity: Case of a heterogeneous fault. *Journal of Geophysical Research: Solid Earth*, 124:8426–8448, 2019.

L. Jin. A hydromechanical-stochastic approach to modeling fluid-induced seismicity in arbitrarily fractured poroelastic media: effects of fractures and coupling. *Tectonophysics*, 826:229–249, 2022.

Y. Y. Kagan. Seismic moment distribution revisited: I. Stastistical results. *Geophys. J. Int.*, 149:520–541, 2002.

T. C. Hanks and H. Kanamori. A moment magnitude scale. *Journal of Geophysical Research*, 84(B5), 1979.

J.D. Eshelby. The determination of the elastic field of an ellipsoidal inclusion and related problems. *Proc. Roy. Soc. series A*, 241:376–396, 1957.

D. I. Garagash and L. N. Germanovich. Nucleation and arrest of dynamic slip on a pressurized fault. *Journal of Geophysical Research*, 117(B10310), 2012.

S. Bourouis and P. Bernard. Evidence for coupled seismic and aseismic fault slip during water injection in the geothermal site of Soultz (France), and implications for seismogenic transients. *Geophys. J. Int.*, 169: 723–732, 2007.

O. Scotti and F. H. Cornet. In Situ Evidence for Fluid-Induced Aseismic Slip Events Along Fault Zones. *Int. J. Rock Mech. Min. Sci. & Geom. Abstr.*, 31(4):347–358, 1994.

Y. Guglielmini, F. Cappa, J.-P Avouac, P. Henry, and D. Elsworth. Seismicity triggered by fluid injection-induced aseismic slip. *Science*, 348, June 2015.

M. M. Scuderi and C. Collettini. The role of fluid pressure in induced vs. triggered seismicity: insights from rock deformation experiments on carbonates. *Scientific Reports*, 6(24852), 2016.

Aki K. Generation and Propagation of G Waves from the Niigata Earthquake of June 16, 1964. Part 2. Estimation of earthquake moment, released energy, and stress-strain drop from the G wave spectrum. *Bulletin of the Earthquake Research Institute*, 44:73–88, 1966.

F. Ciardo and B. Lecampion. Effect of dilatancy on the transition from aseismic to seismic slip due to fluid injection in a fault. *Journal of Geophysical Research: Solid Earth*, 124:3724–3743, 2019.

G. C. P. King, R. S. Stein, and J. Lin. Static stress changes and the triggering of earthquakes. *Bull. Seismol. Soc. Am.*, 84(3):935–953, 1994.

J. Lin and R. S. Stein. Stress triggering in thrust and subduction earthquakes and stress interaction between the sourthern San Andreas and nearby thrust and strike-slip faults. *Journal of Geophysical Research: Solid Earth*, 109(B02303), 2004.

M. R. M. Brown and S. Ge. Small earthquakes matter in injection-induced seismicity. *Geophysical Research Letters*, 45:5445–5453, 2018.

Okada, Y. Internal deformation due to shear and tensile faults in a half-space. *Bull. Seismol. Soc. Am.*, 82: 1018–1040, 1992.

S. Toda, R. S. Stein, P. A. Reasenberg, J. H. Dieterich, and A. Yoshida. Stress transferred by the 1995 Mw = 6.9 Kobe, Japan, shock: Effect on aftershocks and future earthquake probabilities. *Journal of Geophysical Research: Solid Earth*, 103(B10):24543–24565, 1998.

F. Catalli, M.-A. Meier, and S. Wiemer. The role of Coulomb stress changes for injection-induced seismicity: the Basel enhanced geothermal system. *Geophysical Research Letters*, 40:72–77, 2013.

K.-J. Shou, E. Siebrits, and S. L. Crouch. A higher order Displacement Discontinuity Method for three-dimensional elastostatic problems. *Int. J. Rock Mech. Min. Sci.*, 34(2):317–322, 1997.

F. Ciardo, B. Lecampion, F. Fayard, and S. Chaillat. A fast boundary element based solver for localized inelastic deformations. *Int. J. Numer. Meth. Engng.*, pages 1–23, 2020.

F. Catalli, A. P. Rinaldi, V. Gischig, M. Nespoli, and S. Wiemer. The importance of earthquake interactions for injection-induced seismicity: Retrospective modeling of the Basel Enhanced Geothermal System. *Geophysical Research Letters*, 43:4992–4999, 2016.

I. Aavatsmark. An introduction to multipoint flux approximation for quadrilateral grids. *Computational Geosciences*, 6(405-432), 2002.

S. H. Lee, P. Jenny, and H. A. Tchelepi. A finite-volume method with hexahedral multiblock grids for modeling flow in porous media. *Computational Geosciences*, 6:353–379, 2002b.

Wolfram Research, Inc. Mathematica, Version 13.1, 2022. URL `https://www.wolfram.com/mathematica`. Champaign, IL, 2022.

B. Flemisch, I. Berre, W. Boon, A. Fumagalli, N. Schwenck, A. Scotti, I. Stefansson, and A. Tatomir. Benchmarks for single-phase flow in fractured porous media. *Advances in Water Resources*, 111:239–258, 2018.

Utah FORGE - University of Utah. Phase 3a year 2 annual report. Technical report, University of Utah, 2022.